

Development of a CFD-based numerical wave tank of a novel multipurpose wave energy converter

D. Oliveira ^{a,*}, J.P.P.G. Lopes de Almeida ^b, A. Santiago ^a, C. Rigueiro ^c

^a University of Coimbra, ISISE – the Institute for Sustainability and Innovation in Structural Engineering, Portugal

^b University of Coimbra, MARE – Marine and Environmental Sciences Centre, Portugal

^c Polytechnic Institute of Castelo Branco, ISISE – the Institute for Sustainability and Innovation in Structural Engineering, Portugal

ARTICLE INFO

Keywords:

CFD-based numerical wave tank
Physical wave tank
REEFS multipurpose Wave energy converter
Wave-structure interaction

ABSTRACT

The development of new wave energy converters usually involves small-scale experiments in physical wave tanks. The jump to physical models at larger scales is an expensive and time-consuming process that can be supported by computational fluid dynamics (CFD) models. Using the CFD approach, it is possible to numerically simulate complex flows with high accuracy, once validation with experimental data has been carried out. This article describes an approach based on guidelines taken from the literature and adopted to develop and explore the capabilities of a CFD-based numerical wave tank for a novel multipurpose wave energy converter, REEFS. An incremental validation procedure, using experimental data collected with a piston-type wave tank, was adopted; the procedure began with wave-only tests which were followed by wave-structure interaction tests. Snapshots of numerical and experimental approaches were used to analyse fluid flow in the envelope of the REEFS converter. The results demonstrate that the CFD-based numerical wave tank model can adequately simulate the global wave surface profile, as well as local complex phenomena, such as the Venturi aspiration effect, that typically occur near the exterior stay vanes of the device. The results encourage the adoption of this model for future REEFS analysis.

1. Introduction

Ocean waves are an inexhaustible clean source of power with an estimated global potential of more than 2 TW [1]. Despite huge scientific and technological efforts since the 1970s to develop this power source, no commercially competitive solution for wave energy conversion is currently on the market. Consequently, new wave energy converter concepts which aim to overcome traditional disadvantages, such as technological complexity, storm vulnerability, high cost and low productivity, are still being proposed.

1.1. Computational fluid dynamics-based numerical wave tanks

The development of new wave energy converters (WEC) is a process which requires a huge amount of time and money, and only a limited number of inventions reach the full-scale testing phase [2]. At low technology readiness levels, small-scale experiments in physical wave tanks have proven to be suitable and reliable for preliminary proof of

concept, preliminary investigations on the wave energy converter capacities and device performance optimisation [3]. However, physical wave tanks are not only expensive (in terms of equipment, personnel, and space), but also have some limitations which make them laborious tools for WEC development (e.g., time-consuming implementation of setup and experimental testing, finite number of feasible measurement points, instrumentation flow disturbance and measurement errors). Computational fluid dynamics (CFD) based numerical wave tanks (CNWT), which employ standard two-phase Reynolds-averaged Navier-Stokes (RANS) equations using the volume of fluid method to track the position of the free surface, have been widely employed to support the scaling-up of WECs, providing high-fidelity results [4]. Their versatility allows for the study of multiple WEC configurations, at different scales, subjected to an infinite variety of hydrodynamic conditions, with the capacity to promptly output detailed fluid flow characteristics at any location of the numerical domain [4]. Although the use of CNWT for wave energy applications has not yet reached the level of maturity that marine hydrodynamics has, the implementation of

* Corresponding author.

E-mail addresses: daniel.oliveira@uc.pt (D. Oliveira), jppgl@dec.uc.pt (J.P.P.G. Lopes de Almeida), aldina@dec.uc.pt (A. Santiago), constanca@ipcb.pt (C. Rigueiro).

verification (i.e. by coding and calculation) and validation procedures can result in higher confidence in these numerical solutions [5]. An initial code verification process is advised to analyse the correct functioning of the code by evaluating errors and comparing the results with an exact solution. When well-established commercial CFD software (e.g. ANSYS Fluent and Siemens Star-CCM+) is used for WEC experiments, the code can be assumed to have been verified, except in cases where specific code development is needed (e.g. for power take-off and mooring modules). A second calculation verification, in which the error/uncertainty is estimated, is necessary to support analysis of the results when the exact solution is unknown. At this point, two different groups of errors are identifiable: modelling errors and numerical errors. Modelling errors result from simplifications and approximations of reality in the numerical model, in terms of dimensions of computational domains, boundary conditions, simplified WEC body geometries and turbulence models. Numerical errors, on the other hand, fall into three categories: round-off errors, iterative convergence errors, and discretisation errors. Round-off errors are related to hardware quality, which can largely be ignored when using double precision computations [6]. In unsteady flow problems, such as in CNWTs for WEC experiments, time integration is usually performed with implicit schemes where a nonlinear system of equations is solved iteratively at each time step. Iterative errors are generally closely linked to time step size and convergence criterion, which are usually set by defining a minimum residual value for conservation equations and/or limiting the number of iterations per time step. A smaller time step requires less iterations to converge, but also increases the total number of time steps required for the same simulated time. The balance between time step size and number of iterations directly affects model efficiency. It is also important to understand that, as in any iterative process, these errors propagate to the next time step. The choice of the time step used (temporal discretisation) is also dependent on the choice of the mesh size used (spatial discretisation). Both errors should be assessed by analysing different levels of refinement. Wang et al. [6] highlight the importance of assessing the corresponding model accuracy for the next step, with Eça et al. [7] affirming that a global numerical model uncertainty below 5% means that the model can be assumed to be acceptable and reliable. After verification, validation is performed by comparing CNWT numerical results with reference data, which can be analytical data, low-to mid-fidelity numerical data, third-party CFD-based NWT data, or physical wave tank experimental data. According to Windt et al. [4], the use of experimental data is the most common strategy for model validation. When comparing such data with reality, it is important to consider the experimental inaccuracies and scale effects associated to data produced in physical wave tanks, in order to avoid incorrect conclusions.

1.2. Literature review

This section presents a review of previous work considered to be relevant to the current research. The main objective of this literature review is to identify key modelling considerations for the development of CNWT based on RANS equations, in order to use them as guidelines for the present work.

The definition of the numerical wave makers for wave generation and absorption are of upmost importance, and influence all modelling decisions. Gomes et al. [8] developed a 2D CNWT for future WEC analysis, focusing on the comparison of two wave generation methods (the static boundary and dynamic boundary methods). Their study was conducted by performing wave-only test cases with regular waves. A mesh convergence analysis was used to assess model accuracy, obtaining maximum deviations of 1.2% and 5% when comparing numerical and analytical wave amplitude and wave velocity profiles, respectively. Both methods proved to be accurate, with the static boundary method providing a solution in 75% of the time required by the dynamic boundary method. To study the ability to numerically generate and

propagate regular waves in intermediate depths, Silva et al. [9] developed a 2D CNWT using a dynamic boundary method for wave generation and a geometrical beach for wave absorption. Verification and validation procedures were considered in their research. During calculation verification, a maximum relative error of 1% was obtained when comparing numerical and analytical free surface elevation. In the second part of their research, model range applicability was assessed. The CNWT they developed was demonstrated to be accurate within a range of theoretical wave steepness from 0.0033 to 0.0335, presenting a maximum relative deviation of about 3% and 4% for numerical wave height (H) and length (λ), respectively. Marques Machado et al. [10] also investigated the generation (by static and dynamic boundary methods) and absorption (by geometrical beach) of regular progressive waves in a 2D CNWT for future WEC experiments. Spatial and temporal convergence studies were employed for calculation verification. The optimised model was validated against Stokes 2nd order wave theory, showing a maximum deviation of 0.9% from the theoretical elevation of the free surface. A more detailed study was carried out by Miquel et al. [11], who analysed the performance of different combinations of numerical wave makers for the generation and absorption of regular and irregular waves. The accuracy of different techniques was assessed using wave-only (2D) and wave-structure interaction (3D) test cases. Spatial and temporal discretisation was selected on the basis of results from Bihs et al. [12]. The authors concluded that a CNWT using the relaxation method for wave generation and absorption could achieve lower reflection coefficients (<0.1, for regular waves, and <0.01, for irregular waves), but at a high computational cost. A combination of the static boundary method for both wave generation at the inlet, and for wave absorption at the end of the domain, provided higher computational efficiency without reducing the accuracy of the results. Similar work was performed by Windt et al. [13], who present a quantitative comparison and assessment of the different numerical wave makers, and provide generalised assessment metrics and methodologies for both regular and irregular sea conditions to isolate general modelling inaccuracies from those produced by the numerical wave maker. Convergence analyses were used to assess spatial and temporal discretisation uncertainty using mean phase averaged wave height. A maximum relative deviation of 0.10% of the mean phase average wave height from the target value was calculated. The authors highlight the dependency of the performance of the numerical wave maker on the time step used, and assume that it should always be analysed in each case study. With regard to the accuracy of the studied numerical wave makers, the conclusions the authors drew are in accordance with the work of Miquel et al. [11], with the relaxation method providing higher accuracy at high computational cost, while a combination of the static boundary method for wave generation and a numerical beach for wave absorption was demonstrated to be more computationally efficient without compromising the accuracy of the CNWT.

Focusing on wave-structure interaction problems of wave energy sector, Finnegan and Goggins [14] developed a 3D CNWT of a floating truncated vertical cylinder (simplified WEC) and considered both linear deep-water waves and linear waves for finite depths. Initially, convergence studies on spatial and temporal discretisation were performed for calculation verification in a 2D domain, and wave-only simulation cases were considered. The numerical results were qualitatively compared with linear wave theory and wavemaker theory, resulting in “good agreement”. The 3D spatial discretisation was defined on the basis of previous results. The simplified WEC body motion response obtained closely matched (qualitatively) the analytical results. Similar analysis procedures were applied by Kim et al. [15], who developed a 3D CNWT to simulate regular waves and current interaction with a fixed offshore substructure. Their study was divided into three phases with progressively increasing complexity. First, a calculation verification was employed using wave-only test cases and focusing on spatial discretisation of the numerical domain. A maximum numerical deviation of 1.85% from the 2nd order Stokes wave, at the wave crest, was obtained.

A 3D model was then used for the wave-structure interaction analysis, comparing the horizontal wave load on the vertical cylinder with the measurements reported by Chakrabarti and Tam [16] and using the Morison equation for calculation [17]. A maximum relative deviation between experimental, analytical and CFD analysis of around 1% was calculated in a wave-structure interaction test case. For the case of wave and current interaction with the structure, the analytical horizontal load was about 11% lower than that obtained by CFD simulations, demonstrating the importance of nonlinearity effects caused by wave deformation. Several WECs in the literature use a power take-off system that relies on a turbine to convert hydraulic power into shaft mechanical power. To analyse the performance of a WEC turbine, Prasad et al. [18] developed a 3D CNWT. Calculation verification was performed on the basis of a mesh convergence analysis using a 2D model. A maximum relative deviation of 0.2% (compared with experimental data) was calculated for the mean phase averaged wave height. In a second phase, the numerical model, including the turbine, was validated against experimental data. The experiments were conducted using a piston-type wavemaker tank to generate the prototype regular waves. A capacitance type wave gauge was installed at a distance from the wavemaker to measure wave properties (H and T). Instrumentation measurement uncertainties ranging from 1.00% to 2.23% were assessed. A full-scale simulation was then carried out using an optimised CNWT model. The numerical free surface elevation and pressure were compared with theoretical solutions, and good agreement was found by visual inspection of the graphics. The CFD results of the wave power were also compared with field measurements at a location in Fiji, and a maximum deviation of about 3.70% was reported. An extensive validation of a 3D CFD model for the 1:5 scale Wavestar point-absorber, including cases in which an active power take-off system was used, was developed by Windt et al. [19]. Their study was divided into four test cases, based on an incremental validation procedure: wave-only, wave diffraction with fixed WEC, wave radiation in a still tank with the WEC motion being driven by a sinusoidal force, and wave-driven motion of the WEC with power take-off damping simulations. All test cases were validated against physical wave tank data. Spatial and temporal discretisation was determined by following the convergence studies outlined in Ref. [13]. A maximum normalised root mean squared error of the mean phase averaged free surface elevation of about 6% was obtained for wave-only simulation. In the most complete wave-structure interaction model, numerical and experimental data were compared, and maximum normalised root mean squared errors of 13% for surface elevation, 6% for the power take-off cylinder displacement and velocity, 3% for the power take-off force and 19% for instantaneous generated power were obtained. The authors concluded that modelling such a complex physical system is a challenging task. However, their study proved the potential and usefulness of the validated model for future analyses. Another CNWT validation was presented by Windt et al. [20]. These authors compared the results obtained using the CNWT of the 1:20 scale Wavestar WEC against experimental data acquired in a physical wave tank, and outlined the opportunity to combine this study with previous work presented in Ref. [19] in order to develop a future study of scaling effects. As in Ref. [19], a validation procedure with gradual incremental complexity was implemented: this procedure included wave-only, wave excitation force, free decay, forced oscillation, and wave-induced motion cases. Spatial and temporal convergence analyses were performed for the purpose of model verification, and used to determine the required mesh and time step sizes. The comparison between numerical and experimental results showed an acceptable level of agreement, obtaining a maximum normalised root-mean square deviation of 10.99% for the free surface elevation and 6.06% for the floater position. The authors considered the proposed model to have been validated. Following a similar gradual incremental complexity validation procedure, an interesting and innovative multi-domain coupling approach was developed by Di Paolo et al. [21,22] for wave-structure interaction analysis, with the aim of increasing computational efficiency. The

solution presented consisted in decomposing the global domain of the CNWT into partitioned sub-domains, i.e. a 2D region (near field) for wave generation and transformation coupled to a 3D region (far field) for complex wave-structure interaction analysis. In part I [21], wave-only test cases were employed for calculation verification by convergence analysis of spatial and temporal discretisation and validation of the coupling method. Different wave conditions were considered, and a computational acceleration ranging from 1.2 to 5 was observed in comparison to full 3D simulations, without reducing the accuracy of the results. In the majority of cases, the maximum relative errors of the free surface elevation remained below 3%; this slightly exceeded 10% in the worst case, and was below 10% in the analysis of velocity profiles. In a wave-structure interaction analysis, Di Paolo et al. [22] progressively increased the complexity of the problems; they started with the evolution and breaking of waves on a planar beach, proceeded to the study of a wave group impacting on a fixed cylinder installed at the planar beach, and finished by replicating a perforated breakwater WEC in a laboratory experiment. A maximum computational acceleration of 6.25 was achieved. With regard to the wave interaction with the WEC analysis, an error below of 10% was calculated for the wave reflection coefficient, while velocity and pressure measurements were compared qualitatively by the visual inspection of graphics, affirming that there was a “good match between experimental and numerical (coupled models) results”.

A summary of the articles reviewed here, which also includes other interesting studies, is presented in Table 1. This summary can be used to identify and compare the different methodologies, parameters, and recommendations presented by the authors, and constitutes a valuable guide to novel contributions.

In terms of CFD software for the implementation of RANS equations with a volume of fluid approach, ASNSYS (CFX and Fluent) and OpenFOAM were identified as the software packages most often used in the wave energy sector. A different method to capture the free water surface, called the level set method, was implemented by Bihs et al. [12] and Miquel et al. [11] using REEF3D software, which allowed the use of high-order temporal and spatial discretisation to avoid unphysical wave damping. The pressure implicit in the splitting of the operator algorithm (also called PISO) was generally applied to achieve pressure-velocity coupling. An incremental validation procedure has been widely employed for wave-structure interaction problems, starting with wave-only simulations in 2D domains for calculation verification before moving on to complex 3D analyses. It was also noticed that turbulence models were applied in wave-structure interaction problems, especially for the analysis of fixed wave energy converters, without referring to any details (i.e. initial seeding, wall-functions, etc.). With regard to wave generation and absorption, different techniques were chosen by the reviewed authors, with overall good results; this demonstrates that there is no single solution for this problem. Useful generalised assessment metrics and methodologies have been provided by Windt et al. [13]. In the definition of transient (temporal) formulation and advection (spatial) discretisation models, second order schemes proved to be sufficiently accurate for wave generation and propagation in CNWTs, while first order schemes produced wave damping, as demonstrated in Ref. [9]. Model verification based on the quantification of spatial and temporal discretisation errors using convergence studies is the most common practice in the literature. Neglecting high-order terms (with a volume of fluid approach) causes errors, which can be minimized by striking an appropriate balance between mesh and time step sizes. Basic mesh and time step convergence studies which demonstrate that the solution is “mesh/time step-independent” have been identified. However, the use of mesh/time step-independent solutions does not necessarily mean that there are no numerical errors. Evidencing the high degree of uncertainty of this approach, qualitative assessment of convergence is typically performed on the basis of the observation of graphs, or convergence is simply defined without further information. Quantitative assessment based on the relative variation of a given hydrodynamic quantity is always preferable. A structured mesh type,

Table 1

Tabulated overview of the main methodologies, parameters and recommendations identified in the reviewed studies.

Authors	Software	Model	Test cases	Wave generation	Wave absorption	Turbulence	Pressure-velocity coupling	Mesh type	Convergence studies	Spatial discretisation			Temporal discretisation			Assessment of the results
										CPL	CPH	aspect ratio	method	Δt	Maximum C_o	
Gomes et al. [8]	ANSYS Fluent	2D RANS-VOF	Wave-only	SBM DBM	Limited simulation time	Laminar	PISO	Structured	Spatial	102 ^a	14 ^a	1	INA	INA	INA	Quantitative
Silva et al. [9]	ANSYS CFX	2D RANS-VOF	Wave-only	DBM	Geometrical sloped beach	Laminar	Coupled	Structured	Spatial + Temporal	111	10	4.16	fixed	$\leq T/100$	INA	Quantitative
Havn [27]	ANSYS CFX	2D/3D RANS-VOF	Wave-only + WSI	SBM DBM	Geometrical sloped beach	Laminar, k- ϵ , SST k- ω	INA	Structured	Spatial + Temporal	≥ 100	>10	<10	Fixed	$< T/100$	INA	Quantitative
Finnegan and Goggins [14]	ANSYS CFX	2D/3D RANS-VOF	Wave-only + WSI	DBM	Geometrical sloped beach	Laminar	INA	Structured	Spatial + Temporal	10 ^a	9 ^a	7.50 ^a	fixed	$\leq T/50$	INA	Qualitative
Seibt et al. [28]	Ansys Fluent	2D RANS-VOF	WSI	DBM	No method	Laminar	PISO	Structured	Spatial	300 ^a	6 ^a	1	Fixed	T/1500	INA	Quantitative
Kim et al. [15]	ANSYS Fluent	2D/3D RANS-VOF	Wave-only + Wave-current + WSI	DBM	NB + Cell stretching	k- ϵ realizable	PISO	Structured	Spatial	50	30	18	fixed	T/1000	INA	Quantitative
Bihs et al. [12]	REEF3D	2D/3D RANS-LSM	Wave-only + WSI	RZM	NB	k- ω	Chorin's projection	Structured	Spatial + Temporal	80	4	1	Adaptative	–	0.1	Quantitative
Prasad et al. [18]	ANSYS CFX	2D/3D RANS-VOF	Wave-only + WSI	DBM	Cell stretching	k- ϵ	INA	Structured	Spatial	INA	INA	INA	Fixed	T/250	INA	Quantitative
Ransley et al. [29]	OpenFOAM	2D/3D RANS-VOF	Wave-only + WSI	SBM + RZM	RZM	Laminar	PISO	Structured	Spatial + Temporal	INA	36	1	Adaptative	–	0.5	Quantitative
Eskilson et al. [5]	OpenFOAM	2D/3D RANS-VOF	Wave-only + WSI	SBM	RZM	RNG k- ϵ	SIMPLE/PISO (PIMPLE)	Structured	Spatial	INA	5 to 44	INA	Fixed	INA	0.01	Quantitative
Miquel et al. [11]	REEF3D	2D/3D RANS-LSM	Wave-only + WSI	SBM RZM	SBM RZM Geometrical sloped beach	k- ω	Chorin's projection	Structured	Spatial	80 ^a	0.8 to 7.5 ^a	1	Adaptative	–	0.1	Quantitative
Marques Machado et al. [10]	ANSYS CFX	2D RANS-VOF	Wave-only	SBM DBM	Geometrical sloped beach	Laminar	INA	Structured	Spatial + Temporal	111	21	9.57	Fixed	T/200	0.47	Quantitative
Windt et al. [30]	OpenFOAM	2D/3D RANS-VOF	Wave-only + WSI	RZM	RZM + Cell stretching	SST k- ω	SIMPLE/PISO (PIMPLE)	Structured	Spatial + Temporal	INA	INA	1	Adaptative	–	0.5	Quantitative

(continued on next page)

Table 1 (continued)

Authors	Software	Model	Test cases	Wave generation	Wave absorption	Turbulence	Pressure-velocity coupling	Mesh type	Convergence studies	Spatial discretisation			Temporal discretisation			Assessment of the results
										CPL	CPH	aspect ratio	method	Δt	Maximum C_o	
Wang et al. [6]	OpenFOAM	2D/3D RANS-VOF	Wave-only + WSI	RZM	RZM	SST $k-\omega$	SIMPLE/PISO (PIMPLE)	Structured	Spatial + Temporal	37 ^a	30	1.29	Fixed	T/225	INA	Quantitative
Windt et al. [13]	OpenFOAM	2D RANS-VOF	Wave-only	SBM DBM RZM ISM NB	SBM DBM RZM	Laminar	SIMPLE/PISO (PIMPLE)	Structured	Spatial + Temporal	1332	20	1	Fixed	$\leq T/800$ (NWM dependent)	INA	Quantitative
Windt et al. [19]	OpenFOAM	2D/3D RANS-VOF	Wave-only + WSI	SBM + RZM	NB + Cell stretching	Laminar	SIMPLE/PISO (PIMPLE)	Structured	Spatial + Temporal	186	10	4	Fixed	$\leq T/990$	INA	Quantitative
Windt et al. [20]	OpenFOAM	2D/3D RANS-VOF	Wave-only + WSI	RZM + Cell stretching	RZM	Laminar	SIMPLE/PISO (PIMPLE)	Structured	Spatial + Temporal	200	10	0.612 to 2.28	Fixed	T/1400	INA	Quantitative
Di Paolo et al. [21]	OpenFOAM	2D/3D RANS-VOF	Wave-only	SBM, DBM	DBM	Laminar	SIMPLE/PISO (PIMPLE)	Structured	Spatial + Temporal	$\geq 277^a$	10, 12	1, 4	Adaptative	–	0.1, 0.3	Quantitative
Di Paolo et al. [22]	OpenFOAM	2D/3D RANS-VOF	Wave-only + WSI	SBM, DBM	DBM Geometrical sloped beach	Laminar, $k-\omega$	SIMPLE/PISO (PIMPLE)	Structured	Spatial + Temporal	$\geq 292^a$	12, 32	1, 2	Adaptative	–	0.1, 0.3, 0.75	Quantitative Qualitative

^a Estimated based on wave characteristics and mesh sizes. SBM – static boundary method, DBM – dynamic boundary method, RZM – relaxation zone method, ISM – impulse source method, NB – numerical beach, INA – information not available, NWM – numerical wave maker.

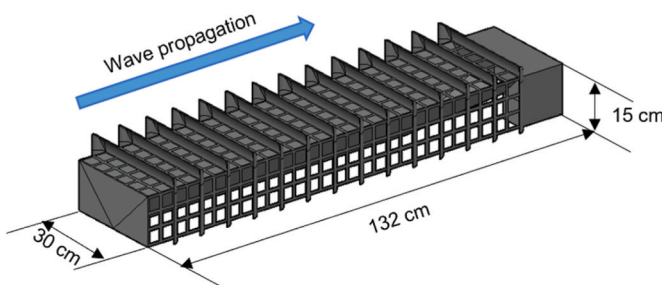


Fig. 1. 3D schematic illustration of the REEFS WEC small-scale model.

refined around the free surface and the structures, has been found to be preferable for ocean wave applications; however, the variety of the results obtained from spatial convergence analysis (number of cells per wavelength, or n.CPL, and number of cells per wave height, or n.CPH) indicate that there is no single solution; this means that it is necessary to perform analyses on a case-by-case basis. Both fixed and adaptative approaches to the temporal discretisation of models have been implemented, the latter being controlled through the Courant Friedrichs Lewy condition and the maximum Courant number. The implementation of a fixed time step should always be followed by the monitoring of the maximum Courant number near the free surface interface, to ensure convergence of the simulation. In both methods, different results have been reported by different authors, indicating that the process is case dependent.

1.3. Scope of the article

This paper presents the development and an exploration of the capabilities of a 3D CNWT model of a novel multipurpose wave energy converter known as REEFS [23–26], Renewable Electric Energy From Sea, with the objective of helping to increase the technological readiness level of this WEC device in the near future. Based on the relevant literature, e.g. Ref. [20], an incremental validation procedure will be adopted; initially, wave-only test cases will be studied by using a 2D model to define spatial and temporal discretisation using convergence studies. A comparison of experimental and CFD results will be used for model validation. A 3D CNWT, developed on the basis of the validated 2D approach, will then be implemented to study wave-REEFS interaction; the CFD results will be compared with experimental data reported in Ref. [25], which was collected at the piston-type wavemaker tank of the Laboratory of Hydraulics, Water Resources and Environment of the Civil Engineering Department of the University of Coimbra. The commercial CFD code ANSYS Fluent will be applied in this study, using a 2.10 GHz Intel® Xeon® Silver 4110 octa-core processor with 64 GB of RAM, combined with a GPU NVIDIA® Quadro™ P2000. Conclusions will then be drawn to determine whether the accomplished CNWT can be considered adequate to support the next development stages of the REEFS multipurpose WEC. It is our belief that this study will contribute to a better understanding of the numerical modelling aspects involved in the wave-structure interaction simulation of this new type of wave energy converter. The CFD approach is also expected to be applied to the development, design and optimisation of a scaled-up REEFS model, focusing not only on detailed analysis of the fluid flow around the structure but also on detailed structural analysis, coupling CNWT



Fig. 2. Laboratory facilities: a) piston wavemaker and b) global view of the wavemaking tank.

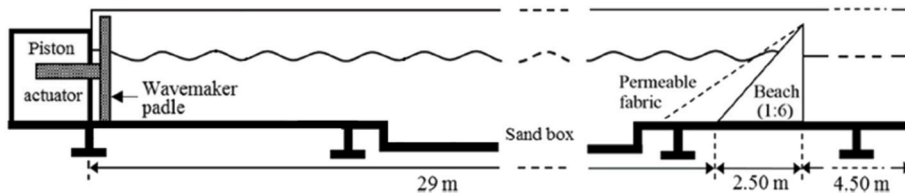


Fig. 3. Schematic illustration of the laboratory piston-type wavemaker tank.

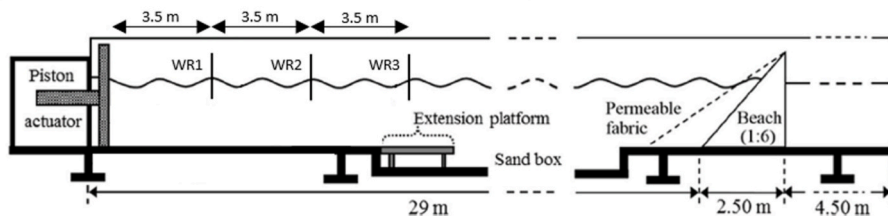


Fig. 4. Schematic representation of the three wave gauges (WR1, WR2, WR3) installed in the piston-type wavemaker tank for the acquisition of free surface elevation data.

Table 2

Wave characteristics in simulated conditions.

Wave-only tests	Wave height H (m)	Water depth h (m)	Wave period T (s)	Wave length λ (m)	Wave steepness H/λ
1	0.014	0.275	0.86	1.067	0.013
2	0.024	0.275	0.86	1.067	0.022
3	0.034	0.275	0.86	1.067	0.032

models with finite element representations of the multipurpose wave energy converter.

2. Materials and methods

2.1. Experimental tests

2.1.1. Physical wave energy converter model

REEFS is a novel multipurpose submerged WEC that combines electric energy production with coastal protection. The device has been under development at the University of Coimbra and was recently granted an international patent. The basic working principle of the device consists of capturing the spatial differentials of kinetic and pressure energy in the water mass just below the wave, to generate an inner flow that drives a fish-friendly low head hydropower turbine. A small-scale physical model (1.5:100), with a length of 132 cm, a width of 30 cm and a height of 15 cm, has already been built. It is made of acrylic plates with 336 square holes of 37 mm per 37 mm, aluminium profiles, 8 mm by 8 mm plastic mesh, plastic film with a 1/12 mm thickness, and iron curved stay vanes. Fig. 1 depicts a three-dimensional view of the described physical model with positioning relative to the direction of wave propagation.

Experimental tests for proof of concept were conducted in the piston-type wavemaker tank at the Laboratory of Hydraulics, Water Resources and Environment of the University of Coimbra (LHWRE-UC), using the small-scale physical model (1.5:100), as reported in Ref. [23]. The same facilities were used to assess, separately, two device functionalities. The capacity of REEFS to produce electric energy was investigated by Lopes de Almeida et al. [24] by carrying out wave-to-water power tests, coupling a power take-off unit to the already existing REEFS model, and

considering regular waves and normal operating conditions. More recently, the potential of REEFS for shore protection was evaluated by Lopes de Almeida and Santos Martinho [25], based on measurements of wave energy dissipation in the device.

2.1.2. Laboratory facilities

The wave tank of the LHWRE-UC is 36 m long, 1 m in width and 1.2 m in height, with a deeper zone (+0.20 m) at the centre of the tank. It is equipped with a piston-type wavemaker (see Fig. 2 and Fig. 3) for wave generation, and a sloped beach to mitigate wave reflection at one end. DHI Wave Synthesizer software [31] was used to generate wave profiles, which were transferred to the DHI AWACS active control unit that governs the movement of the piston wavemaker. Regular and irregular sea states can be generated using this equipment. The side walls and the bottom of the tank are made of tempered glass, allowing visual data acquisition.

2.1.3. Wave-only test cases

A preliminary experimental analysis with wave-only test cases was conducted to assess the functioning of the piston wavemaker. Three twin-wire resistive HR Wallingford wave gauges [32] were installed along the tank (see Fig. 4: $x = 3.5$ m (WR1); $x = 7.0$ m (WR2); $x = 10.5$ m (WR3)) to register the free surface elevation time series and evaluate incoming wave properties (H and T). The wave gauges were connected to a personal computer through a HR Wallingford wave probe monitor system [32], and the HR Waves – Data acquisition and analysis software program [33] was used for calibration, data processing and monitoring. An extension platform was needed to ensure the uniform depth of all the wave gauges. A sloped beach was used in a downstream position in the tank to mitigate wave reflection.

The generation and propagation of three regular waves, with a period of 0.86 s and wave heights varying of 0.014 m, 0.024 m and 0.034 m, based the work presented in Ref. [25], was analysed. Table 2 summarises the respective characteristics of these waves.

In the first stage, the movement of the paddle wavemaker was monitored using a linear variable differential transducer. According to Dean and Dalrymple [34], for regular waves, a transfer function can be used to relate the piston wave maker stroke (S), the water depth (h) and the wave characteristics (H , k),

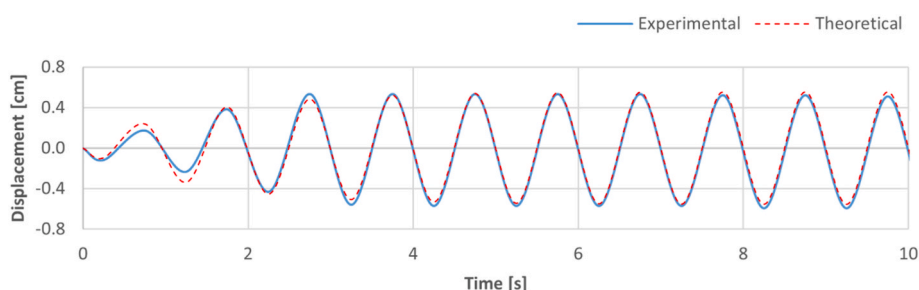


Fig. 5. Comparison of the experimental (blue) and theoretical (red) displacement of the piston wavemaker paddle, for wave-only test case 1.

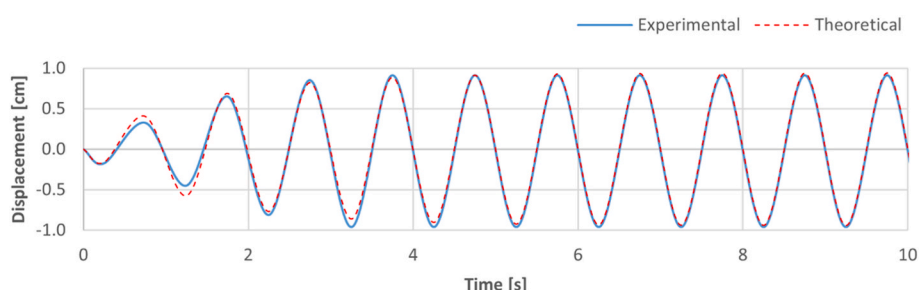


Fig. 6. Comparison of the experimental (blue) and theoretical (red) displacement of the piston wavemaker paddle, for wave-only test case 2.

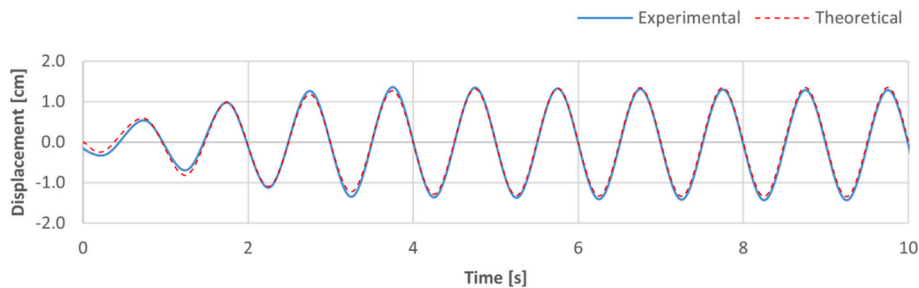


Fig. 7. Comparison of the experimental (blue) and theoretical (red) displacement of the piston wavemaker paddle, for wave-only test case 3.

$$\frac{H}{S} = \frac{2(\cosh(2kh) - 1)}{\sinh(2kh) + 2kh} \quad (1)$$

where k is the wave number. Based on the calculated theoretical stroke, the experimental wavemaker paddle displacement time series were compared with piston wavemaker theory by superimposition,

$$x(t) = \frac{S_0}{2} \left(1 - e^{-\frac{St}{2}}\right) \sin(\omega t), \quad (2)$$

where x is the distance along the longitudinal direction [m], t is time [s], and S_0 is maximum displacement. The results are shown in Figs. 5 to 7.

The experimental averaged strokes were then calculated and compared with the theoretical solution, along with the corresponding averaged periods. The maximum deviation from the theoretical solution was in the order of 3% in wave-only test case 1 (see Fig. 5). The results showed that the wave generation system was well calibrated.

In the second stage, the accuracy of the experimental setup was assessed by comparing the experimental free surface elevation time series (Figs. 8 to 10) against the theoretical wave profile using Stokes' 2nd order theory [35],

$$\eta = \frac{H}{2} \cos(kx - \omega t) + \frac{\pi H}{8} \frac{H}{\lambda} \frac{\cosh(kh)}{\sinh^3(kh)} \times [2 + \cosh(2kh)] \cos[2(kx - \omega t)] \quad (3)$$

In all experiments, data collection was begun with the free surface at rest. The experimental free surface elevation time series exhibited an initial transient state. This transient state was caused by the initiation of the wavemaker, which produces local acceleration in fluid that was initially in a hydrostatic state. The presence of noise in the signals collected was also identified during this period; noise faded with time (i.e. with the increase of free surface elevation), being more significant in test case 1 (Fig. 8) as compared with test cases 2 (Fig. 9) and 3 (Fig. 10). The vibrations caused by the wavemaker equipment can introduce small water surface instabilities, which may have been registered by the wave gauges. After this initial period, a steady state flow was achieved, with regular waves presenting the theoretically expected specified characteristics (e.g. a good match between the red and blue curves). A good agreement was obtained for the mean phase averaged wave height and the period that presented maximum deviations with the reference values of about 3.6% and 0.7%, respectively, for the wave-only test case 1. These maximum deviations were identified after an initial period of 25 s. These results were also in accordance with typical experimental uncertainties reported in Ref. [4].

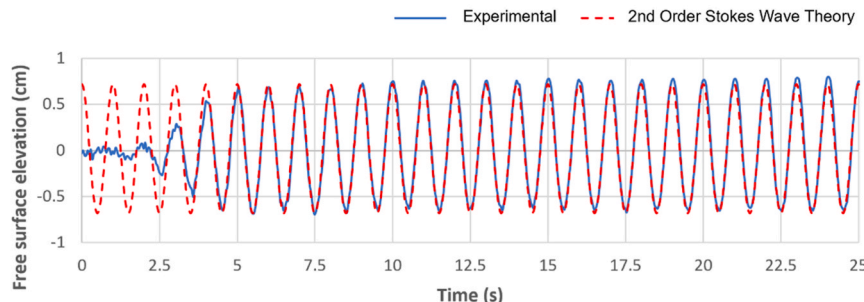


Fig. 8. Comparison of free surface elevation (blue) with analytical solution (red) from 2nd order Stokes' wave theory, at 3.5 m downstream from the piston wavemaker paddle (WR1), for a wave with $T = 0.860$ s, $H = 0.014$ m at $d = 0.275$ m (wave-only test case 1).

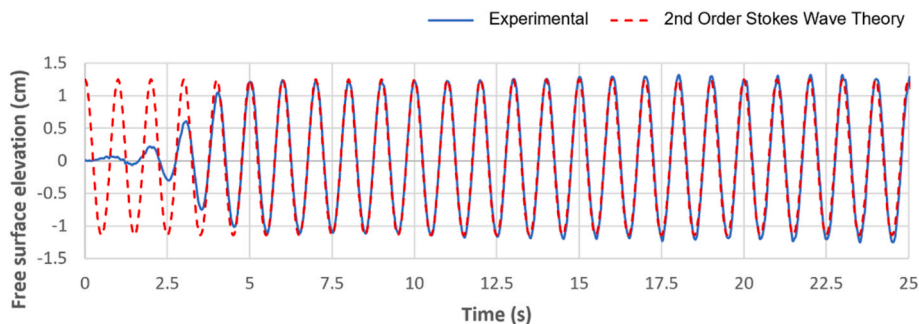


Fig. 9. Comparison of free surface elevation (blue) with analytical solution (red) from 2nd order Stokes' wave theory, at 3.5 m downstream from the piston wavemaker paddle (WR1), for a wave with $T = 0.860$ s, $H = 0.024$ m at $d = 0.275$ m (wave-only test case 2).

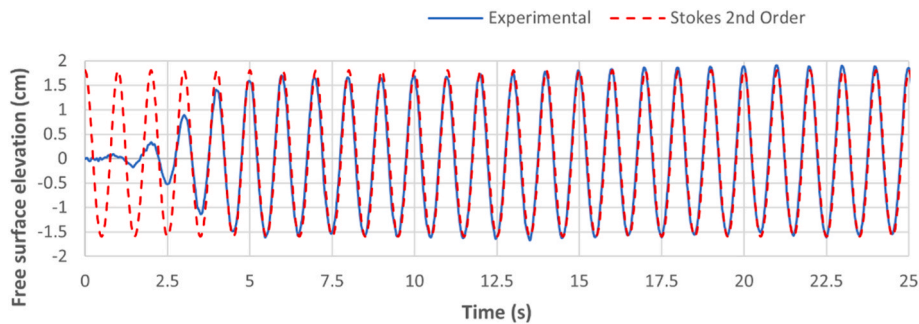


Fig. 10. Comparison of free surface elevation (blue) with analytical solution (red) from 2nd order Stokes' wave theory, at 3.5 m downstream from the piston wavemaker paddle (WR1), for a wave with $T = 0.860$ s, $H = 0.034$ m at $d = 0.275$ m (wave-only test case 3).

2.1.4. Wave-structure interaction test cases

For the exploration of the 3D CNWT model capabilities for wave-structure interaction test cases, the experimental data collected by Lopes de Almeida and Martinho [25] was used. The test campaign was developed at LHWRE-UC with the aim of evaluating the coastal protection potential of the REEFS device using a (1.5:100) small-scale model of the REEFS device. Lopes de Almeida and Martinho [25] analysed the potential of the novel multipurpose wave energy converter for shore protection. The reduction of incoming wave energy density, from upstream to downstream of the device, was used as the guiding parameter. The variation of the free surface elevation was acquired using a laboratory setup with four twin-wire resistive wave gauges, installed at P0, P1, P2, and P3 positions, as schematically illustrated in Fig. 11 and Fig. 12.

Small-scale modelling followed the approach adopted in Refs. [23, 24], i.e. typical values for sea wave heights and periods in the western Portuguese coast near Figueira da Foz were converted using the geometrical scale of ($e_L = 1.5 : 100$) and the time scale of ($e_T = \sqrt{e_L} \cong 1.22475 \times 10^{-1}$), assuming Froude similarity. The resulting model periods varied between 0.73 s, 0.86 s, 0.98 s, 1.10 s, 1.35 s, and 1.45 s, plus an exploratory period of 2.08 s, and model wave heights varied from $H = 1$ cm to $H = 9$ cm. The water depth was $d = 27.5$ cm. The study of coastal protection energy dissipation potential focused on storm conditions, not on operating conditions. Therefore, the power take-off unit was removed from the model and the inner flow was blocked to replicate prototype turbine shutoff. The waves resulting from the energy dissipation process over the REEFS model were irregular (e.g., curve (b) in Fig. 13), which necessitated the use of a frequency (f) domain approach.

A Discrete Fourier Transform (DFT) was implemented to obtain the wave energy spectral density function $S(f)$ using the free surface elevation time series collected at the wave gauge locations. The Fourier Analysis function available in Microsoft Excel [36] was used in these computations. Evaluation of the wave energy dissipation was achieved by comparing the upstream and downstream zero order moments, m_0 , of the respective wave states,

$$m_0 = \int_0^\infty f^0 S(f) df = \int_0^\infty S(f) df \quad (4)$$

The m_0 values reported in Ref. [25] were organised by joining the results obtained with different wave heights but with a common wave period. In Fig. 14, a graph organised in a similar way for wave-only tests with $T = 0.86$ s and numerical wave heights from approximately 0.02 m until 0.06 m is presented. This graph was computed using the experimental database of the test campaign described in Ref. [25].

2.2. Numerical wave tank

The development of a CNWT requires the implementation of adequate mathematical models, the solution of which is approximated by discretisation of space (domain) and time, moving from a continuum problem to a discrete level. To ensure the correct prediction of fluid motion, the numerical solution method should have certain properties: consistency, stability, convergence, conservation of laws, boundedness, realisability, and accuracy [37]. In this study, the well-established CFD code ANSYS Fluent [38], version 19.2, was used to implement a 3D CNWT for wave-structure interaction analysis. The RANS equations combined with volume of fluid method, as proposed by Hirt and Nichols [39], were applied to solve the two-phase flow problem. A cell-centred finite volume method using a mosaic poly-hexacore mesh type, where the average variable value is stored in the centre of each cell, was employed, approximating the differential equations in order to obtain a system of algebraic equations for the variables at the numerical mesh in space and time. The setup of the CNWT was based on the papers reviewed in Section 1, which provided useful guides.

2.2.1. Governing equations and solution methods

The RANS equations express the conservation of mass in Eq. (5), and momentum for an incompressible fluid in Eq. (6) [19],

$$\nabla \cdot \rho \mathbf{u} = 0 \quad (5)$$

$$\frac{\partial \rho \mathbf{u}}{\partial t} + \nabla \cdot \rho \mathbf{u} \mathbf{u} = -\nabla p + \nabla \cdot \mathbf{T} + \rho \mathbf{f}_b, \quad (6)$$

where t denotes the time, \mathbf{u} the fluid velocity, ρ the fluid density, p the fluid pressure, \mathbf{T} the stress tensor and \mathbf{f}_b external forces, such as gravity. In all simulations, the PISO pressure velocity coupling algorithm was set

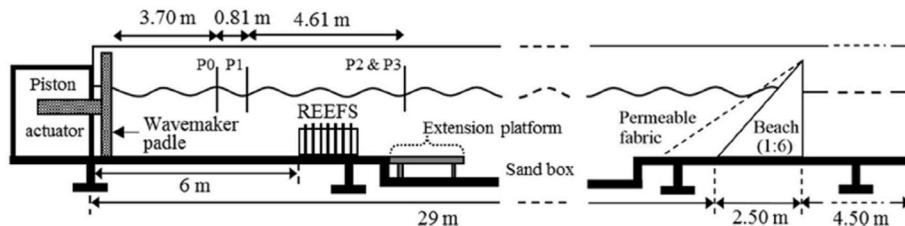


Fig. 11. Right side view illustration of the experimental setup used to evaluate wave energy dissipation in the REEFS small scale model, where P0, P1, P2 and P3 represent wave gauges (vertical scale was increased for better understanding of the drawing), according to Lopes de Almeida and Santos Martinho [25].

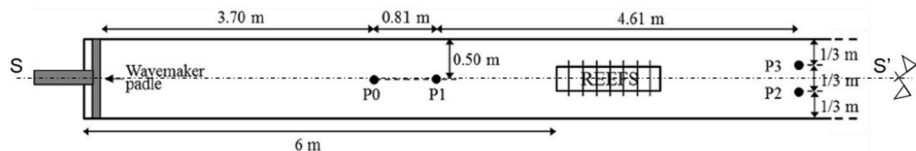


Fig. 12. Top view zoom illustration of the first 9.1 m of the experimental setup used to evaluate wave energy dissipation in the REEFS small scale model, where P0, P1 and P3 represent wave gauges and the dash-dotted line SS' represents a symmetry axis, adapted from Ref. [25].

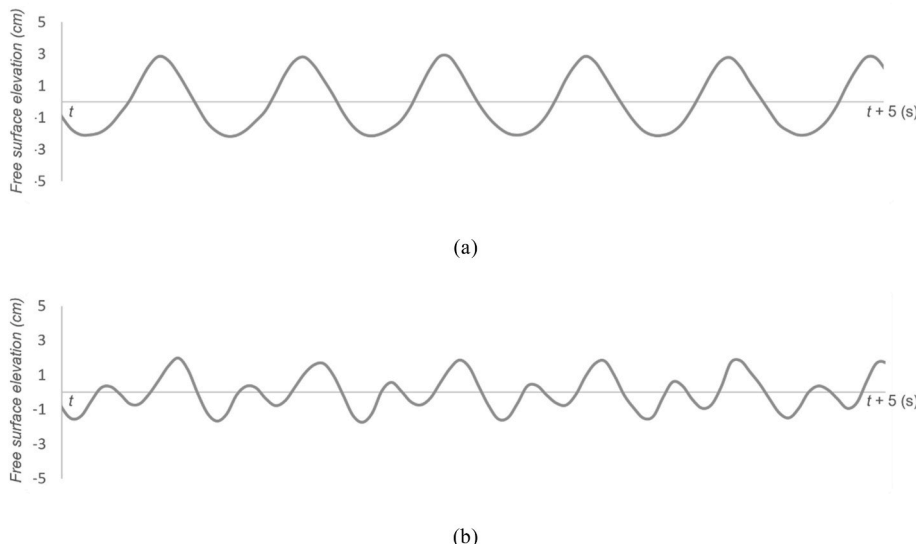


Fig. 13. Experimental (a) upstream (P1) regular wave profile and (b) downstream (P2) random 5 s sample of wave profile, for an incident wave with period, $T = 0.86$ s, height, $H = 0.05$ m and depth, $d = 0.275$ m, drawn using the database of the test campaign described in Ref. [25].

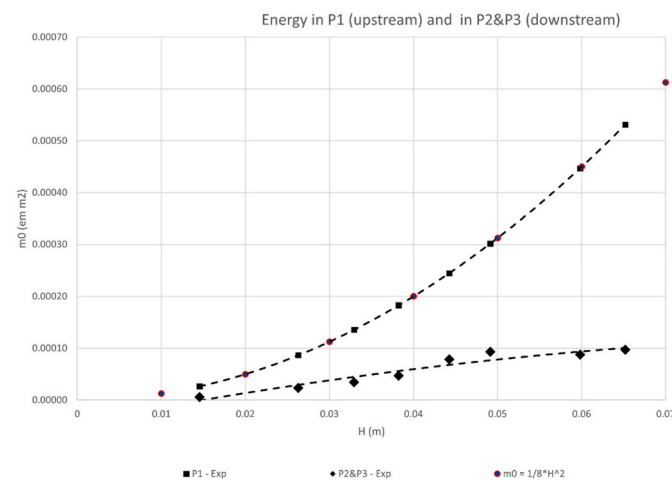


Fig. 14. Experimental upstream (P1-Exp) and downstream (P2&P3 - Exp) values of m_0 for a wave with a period of $T = 0.86$ s, height of $H = 0.05$ m and depth of $d = 0.275$ m, impinging over a REEFS model with exterior stay vanes. This graph was computed using the database of the test campaign described in Ref. [25].

to solve the RANS in a segregated manner, which allows the use of larger time steps in transient simulations, as demonstrated in Refs. [8,15]. The volume of fluid method adds a governing equation to the mathematical model to determine the volume fraction of each fluid within each cell [19],

$$\frac{\partial \alpha_{VF}}{\partial t} + \nabla \cdot \alpha_{VF} u + \nabla \cdot [u_r \alpha_{VF} (1 - \alpha_{VF})] = 0 \quad (7)$$

$$\varphi = \alpha_{VF} \varphi_{water} + (1 - \alpha_{VF}) \varphi_{air} \quad (8)$$

where α_{VF} represents the volume fraction of water, u_r the relative velocity between phases, and φ a specific fluid quantity for an air-water problem. The least squares cell based (LSCB) and the body force weighted (BFW) schemes were employed for gradient and pressure interpolations, respectively. The second order upwind scheme was implemented to obtain the face fluxes whenever a cell was filled with water or air (momentum interpolation). When a cell was near the air-water interface, the modified HRIC scheme, proposed by Ref. [40], was used to calculate the position of the free surface within the cell, as in Ref. [15]. The full performance of this method was achieved by limiting the maximum Courant number to 0.3, which ensured low diffusion of the water-air interface by blending the bounded upwind and bounded downwind schemes. The second order implicit time integration scheme was defined for time discretisation of the governing equations throughout the computational domain. Laminar flow conditions were assumed for waves-only test cases. For wave-structure interaction test cases, the SST $k - \omega$ turbulence model was used with good accuracy in the near wall boundary layer and far wall regions, as reported in Refs. [4, 41]. A maximum residual value of 10^{-5} was defined to minimise iterative errors and to ensure solution convergence. Round-off errors were avoided by performing double-precision computation. A detailed description of the selected solution methods can be found in Ref. [42].

2.2.2. Wave generation and absorption

The accuracy and efficiency of a CNWT is strictly linked to the performance of the numerical wave makers. The selection of the appropriate numerical wave maker is case dependent, and it should be supported by an assessment of the performance of the available numerical wave makers in a specific CFD toolbox [13]. Based on the reviewed literature, both static and dynamic boundary methods showed

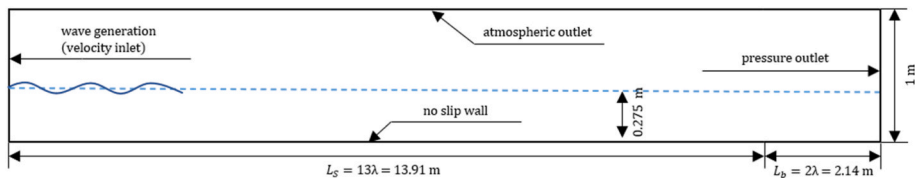


Fig. 15. Schematic of the 2D CNWT for wave-only test cases (vertical scale is increased for better understanding of the drawing).

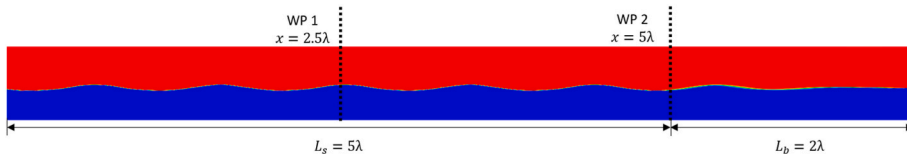


Fig. 16. α_{VF} scalar field in the generic 2D CNWT, at $t_s = 25s$, with location of the two WPs (blue colour corresponds to the water volume, with $\alpha_{VF} = 1$, and red colour to the air volume, with $\alpha_{VF} = 0$).

good accuracy in the generation of regular waves. However, the high computational costs associated with implementing the dynamic boundary method were clearly identified, and the static boundary method was thus chosen. The static boundary method defines the velocity and the free surface elevation as Dirichlet boundary conditions at the numerical wave maker boundaries of the CNWT. The wave theory (or user defined time series) was used to define the wave characteristics at the wave generation boundary. In ANSYS Fluent code, the static boundary method is available in the open channel flow and the open channel wave boundary condition volume of fluid sub-models [42]. The generation of incoming waves is achieved by defining a velocity inlet boundary condition coupled with open channel wave boundary condition. This static boundary method allows the generation of (i) regular waves (Airy, Stokes up to 5th order, 5th order cnoidal and 5th order solitary) and (ii) irregular sea states by a superposition of regular waves or by well-known wave spectrums (Pierson-Moskowitz, Jonswap and TMA).

For wave absorption, a pressure outlet boundary condition was applied to the far field boundary, allowing the propagating waves to exit the computational domain. The mean free surface level was kept constant at this boundary to ensure that no build-up of fluid occurred downstream of the CNWT. Similar to the studies of Kim et al. [15] and Windt et al. [20], a damping zone with a numerical beach and cell stretching, which provides additional damping and reduces the total number of cells, was implemented in the vicinity of the far field boundary to mitigate wave reflection. For the numerical beach zone, damping sinks were introduced to the RANS momentum equation, which were equal to zero in the simulation zone and gradually increased over the length (linear damping) and height (quadratic damping) of the damping zone. According to Perić and Abdel-Maksoud [43], linear (f_1) and quadratic (f_2) damping resistances must be adjusted according to the wave parameters. Considering the results obtained by Perić and Abdel-Maksoud [43], practical recommendations to calculate effective f_1 and f_2 were presented:

$$f_1 = \Psi_1 \omega \quad (9)$$

$$f_2 = \Psi_2 \lambda^{-1} \quad (10)$$

with $\Psi_1 = \pi$, ω = wave frequency, and $\Psi_2 = 2\pi \cdot 10^2$.

Considering the wave conditions of the present study, where $T = 0.86$ s, $d = 0.275$ m, and $\lambda = 1.07$ m, $f_1 \cong 23$ and $f_2 \cong 589$ was defined in all simulations. Variations of computational grid, wave steepness and beach length were also considered in Ref. [43], but only the last parameter showed significant impact on the K_r value. A beach length of $1.5\lambda \leq L_b \leq 2\lambda$ is suggested by Perić and Abdel-Maksoud [43] for an efficient numerical absorption of regular and irregular waves. A

reflection analysis, based on the three point method as presented in Ref. [44], was performed to determine the accuracy of the numerical beach in absorbing incoming waves. A generic 2D computational domain with a simulation zone (L_s) for data acquisition, with a length of $L_s = 5\lambda$ coupled to a numerical beach with a length of $L_b = 2\lambda$, was used for the analysis. Considering the upper limit of Stokes 2nd order validity domain, Stokes 2nd order waves with a wave height of 0.05 m, wave period of 0.86 s and propagating at a water depth of 0.275 m were generated using the static boundary method. After achieving a stabilised fluid flow, an average wave height deviation of 0.9 mm was obtained, resulting in a reflection coefficient of $K_r = 1.8\%$. Therefore, the numerical beach was shown to be adequate for the present study.

2.2.3. Computational domain

Two different computational domains were used to accomplish the proposed objectives. For wave-only tests, only bi-dimensional waves were considered because the corresponding tri-dimensional wave would be cylindrical, propagating parallel to the longitudinal wave tank direction. Thus, a 2D CNWT was implemented (Fig. 15), reproducing the physical wave tank zone where experimental data was acquired (Fig. 4).

The definition of the spatial and temporal discretisation steps was addressed by performing convergence studies, using the generic 2D CNWT from the wave reflection analysis described in Section 2.2.2. With regard to spatial discretisation, the use of a uniform dense transversal mesh is not advisable due to the high number of cells and consequent high computational costs. A vertical mesh configuration based in layers with different refinement levels and mesh grading, parameterised by CPH, is recommended [13]. A refined zone around the free surface interface of about twice the wave height (2.H) was typically implemented in the reviewed studies. On the other hand, in the wave propagation direction, a uniform spatial discretisation solution parameterised by CPL was identified.

Based on these assumptions and the reviewed literature (*i.e.*, Section 1), a convergence study was conducted which considered different vertical (5, 10 and 20 CPH) and longitudinal (25, 50, 75, and 100 CPL) mesh sizes in the interface region, which correspond to a variation of the cell aspect ratio from 1.1 to 17.1. The free surface elevation was monitored at the middle (WP1) and at the end (WP2) of the simulation zone of the generic 2D CNWT (e.g. Fig. 16), and z-positions were extracted from the water volume fraction $\alpha_{VF} = 0.5$ iso-surface, as proposed by Windt et al. [13]. Velocity profile was also cumulatively monitored at the WP1 position. The temporal discretisation was kept constant at $T/200$, ensuring the correct analysis of the mesh size. Stokes 2nd order waves, with a wave height of 0.05 m, a period of 0.86 s, and propagating at a water depth of 0.0275 m, were generated using the static boundary method. All simulations were initiated with a flat-water

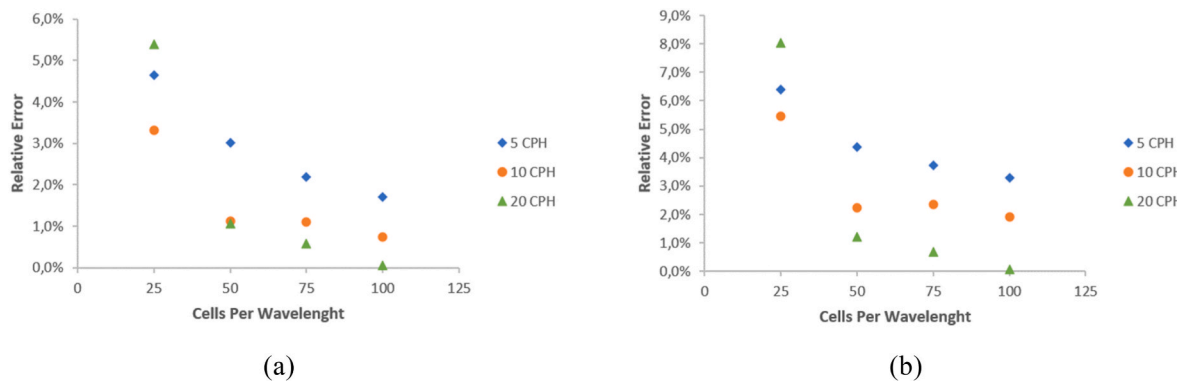


Fig. 17. Spatial convergence study results: wave height relative error at WP1 (a) and WP2 (b), for Stokes 2nd order reference waves with $T = 0.860$ s, $H = 0.050$ m at $d = 0.275$ m (wave-only test case). Time step: $T/200$.

surface condition and performed for a simulated time of $t_s = 25$ s. Transient effects were avoided by collecting the data only after steady flow was achieved ($t_s \geq 15$ s).

The numerical mean phase averaged wave height, \bar{H}_k , was used for the convergence study. The \bar{H}_k was obtained by initially splitting the free surface elevation time series at WP1 and WP2 into zero crossing periods, determining the corresponding wave heights, and finally computing the global mean. The relative deviation of the \bar{H}_k from the reference theoretical value was adopted as the guiding criterion. This criterion was designated by wave height relative error (R):

$$R = \frac{\epsilon_{\text{Numerical}} - \epsilon_{\text{Reference}}}{\epsilon_{\text{Reference}}} \quad (11)$$

Fig. 17 shows the results of the wave height relative error at WP1 (a) and WP2 (b). Global convergence trends were verified from the results at both locations. As expected, higher quality meshes show lower R values, but also increase the CPU time (Fig. 18) due to the increase in the total number of cells. A good compromise between minimising CPU time and ensuring the quality of the results is recommended. Cumulatively, results at both locations (WP1 and WP2) must be analysed to identify possible numerical wave damping while travelling through the simulation zone.

Based on the results at WP1 (Fig. 17 (a)), a minimum mesh refinement of 10 CPH and 50 CPL (aspect ratio of 4.27) was demonstrated to be accurate enough, with $R = 1.1\%$. However, an increase of the relative

error to $R = 2.3\%$ was verified at WP2 (Fig. 17 (b)), confirming that the waves were being numerically damped at a rate of 0.48% per wavelength. Extrapolating the total wave damping for the total length of the 2D CNWT (Fig. 15), this would correspond to a total numerical wave damping of 6.64% , which is considered high for the present case study. The finest mesh configuration, with 20 CPH and 100 CPL and an aspect ratio of 4.27, which results in almost null R values at both locations, was chosen. The corresponding free surface elevation time series (Fig. 19) and horizontal velocity profiles over the water column (Fig. 20), both at WP1, were superimposed on the corresponding Stokes 2nd order wave theory. A good match between the numerical variation of the free surface elevation and the target solution was verified. Regarding the wave velocity profiles, extreme deviations of -4.3% and 3.1% were obtained in the vicinity of the free surface, at the crest and at the trough respectively. These results corroborate the previous conclusion that there is good agreement between the numerical and theoretical reference values.

A temporal convergence study was also carried out, following a procedure similar to the spatial convergence study. The phase averaged wave height was analysed at WP1 using temporal discretisation steps of $T/100$, $T/200$, and $T/400$. The relative errors obtained with the larger time step and the smaller time step were $R = 4.64\%$ and $R \approx 0\%$, respectively. Since no differences were identified between time steps $T/200$ and $T/400$, the larger time step was implemented, avoiding excessive computational costs. A maximum Courant number of 0.27 (<0.3) was registered, ensuring the full performance of the modified HRIC scheme, as previously mentioned.

For the wave-structure interaction analysis, a 3D CNWT was used to reproduce the experimental setup illustrated in Fig. 12, where a longitudinal symmetry plane can be identified. A preliminary analysis was performed to exploit this property, which allowed a reduction of the overall cell count to about half, and a consequent reduction in calculation time. Numerical simulations of a fully 3D domain (Fig. 21a) and a 3D domain with a symmetry plane (Fig. 21b) were performed to analyse

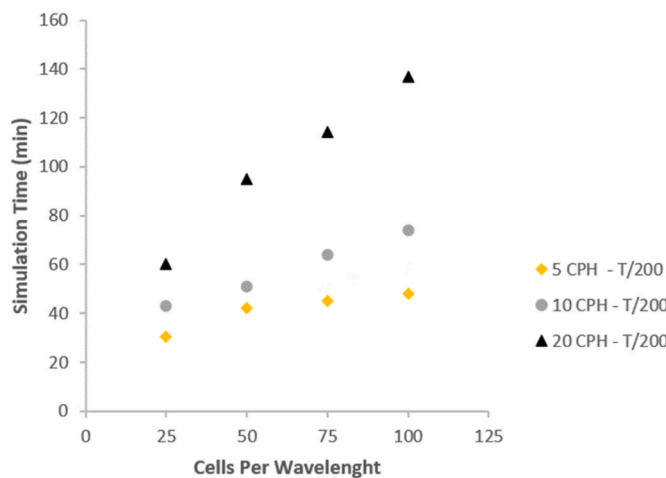


Fig. 18. Comparison of computational costs with different levels of refinement around the free surface ($2H$), for a simulated time of 25 s, generating Stokes 2nd order reference waves with $T = 0.860$ s, $H = 0.050$ m at $d = 0.275$ m (wave-only test case). Time step: $T/200$.

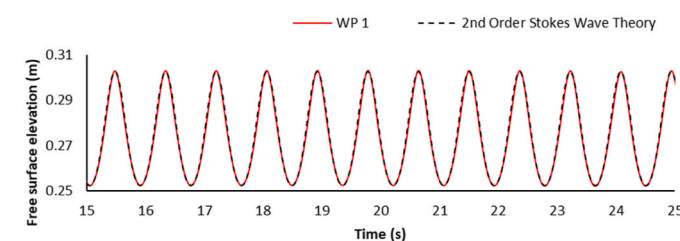


Fig. 19. Variation of the free surface elevation with time at WP1, computed with CNWT (red continuous line) and with Stokes 2nd Order Wave Theory (dark dashed line), with $T = 0.860$ s, $H = 0.050$ m at $d = 0.275$ m (wave-only test case). Mesh refinement: 20 CPH and 100 CPL. Time step: $T/200$.

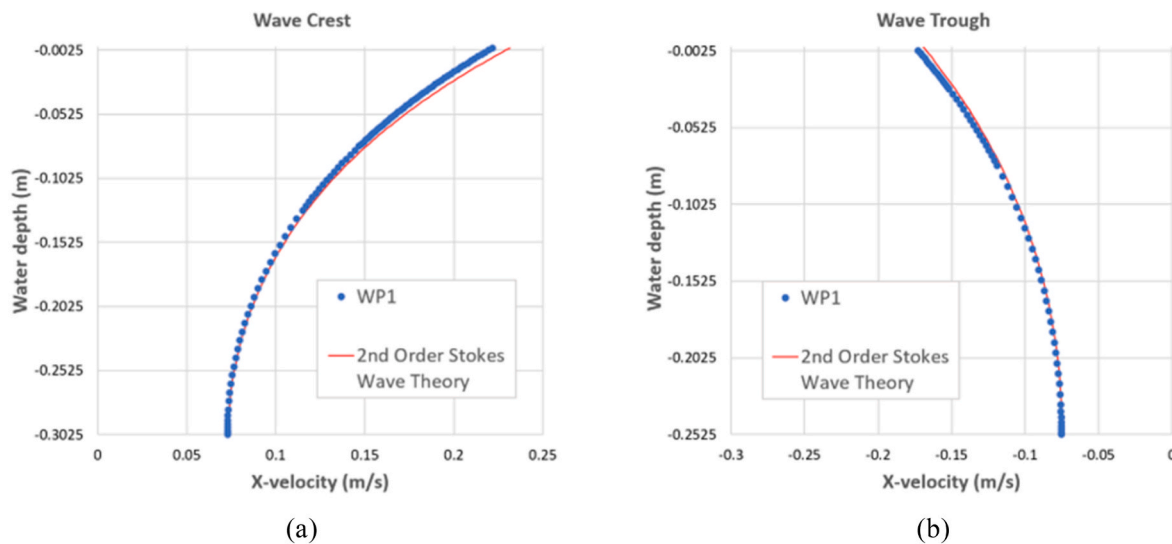


Fig. 20. Horizontal velocity profile at WP1, for a wave crest (a) and for a wave trough (b), computed with CNWT (blue dots) and with 2nd order Stokes wave theory (red line) for $T = 0.860$ s, $H = 0.050$ m and $d = 0.275$ m (wave-only test case). Mesh refinement: 20 CPH and 100 CPL. Time step: T/200.

the validity of this assumption for the present study. The spatial and temporal discretisation solutions from previous convergence studies were employed. The free surface elevation was monitored one wavelength ($\lambda = 1.07$ m) downstream the REEFS device. Both free surface elevation time series are superimposed in Fig. 22. A phase lag was observed after approximately 3.7 s of simulated time, followed by an increase in the wave crest on the symmetric 3D domain at $t \approx 5.2$ s. The implementation of the symmetric boundary condition does not replicate the real balanced right and left lateral wall reflection, which leads to a more unstable initial wave profile that converges after some seconds to the wave profile and celerity of the fully 3D model. However, after this peak, the variations of free surface elevation showed similar behaviour, with a deviation of the mean phase averaged wave height of approximately 3.5%. Considering the doubling of computational costs when using the fully 3D domain, and the proposed objectives for the present study, a decision was taken to consider the symmetric approach.

The final 3D mesh configuration was generated using a mosaic polyhexacore mesh type [38] with approximately 4.2 million cells. In Fig. 23, details of 3D CNWT model mesh configuration are presented.

3. Results and discussion

In this section, the numerical results of the tests introduced in Section 2 are presented and compared with the experimental data to discuss the validation of both 2D and 3D CNWT models.

3.1. Wave-only tests

In the wave-only tests, three numerical simulations corresponding to the tests presented in Table 2 were performed to validate the 2D CNWT. The numerical wave gauges were implemented at the same positions of the corresponding experimental wave gauges (i.e., WR1, WR2 and WR3 in Fig. 4). As with the methodology implemented in convergence studies, the variation of the free surface elevation was monitored by analysing the variation of the z-position of the water volume fraction $\alpha_{VF} = 0.5$ iso-surface. All numerical models were run for a total simulation time of $t_s = 20$ s, which proved to be adequate to achieve a steady flow. The experimental and numerical free surface elevation time series in all wave gauges were superimposed and the corresponding relative deviances used as the guiding criteria. Globally, numerical results exhibit a remarkable agreement with experimental data in all test cases. In Figs. 24–27, the results from wave-only test case 1 are presented. Visual inspection of the graphics shows that the numerical transient flow matches the measured experimental data quite well (in terms of periodicity and magnitude). After an initial period, the transient flow decreased and tended to a steady state flow, as expected. Quantitatively, a maximum relative deviation of experimental and numerical \bar{H}_k values of the about 7% was identified in wave-only test case 1. This could partially result from some interference by the incoming and reflected waves from the physical beach of the wave tank. The relative deviation from experimental data does not exceed the 10% mentioned in Ref. [4] as the upper acceptable limit for validation.

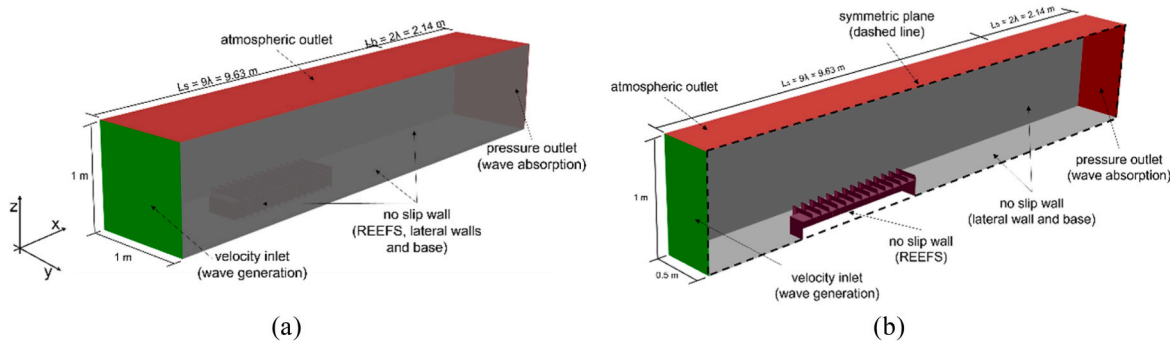


Fig. 21. Layouts of the (a) fully 3D CNWT domain and (b) symmetric 3D CNWT domain, including boundary conditions, for the wave-structure interaction test cases.

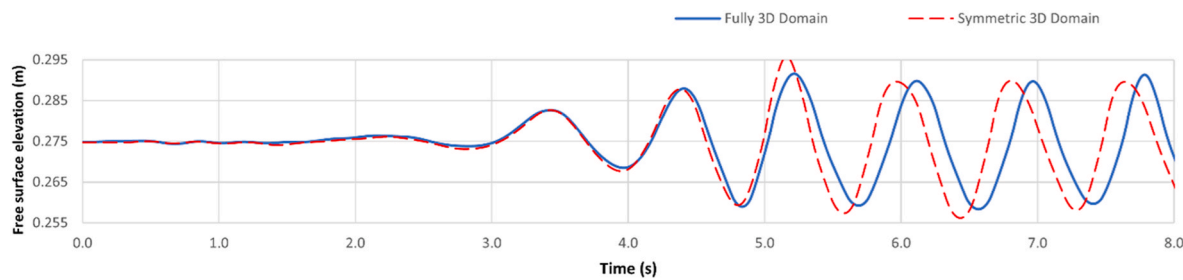


Fig. 22. Comparison of the results from numerical simulations with fully 3D domain (blue continuous line) and with 3D domain considering the symmetry of the problem (red dashed line), generating 2nd order Stokes waves with $T = 0.860$ s, $H = 0.050$ m and $d = 0.275$ m. Mesh refinement: 20 CPH and 100 CPL. Time step: T/200.

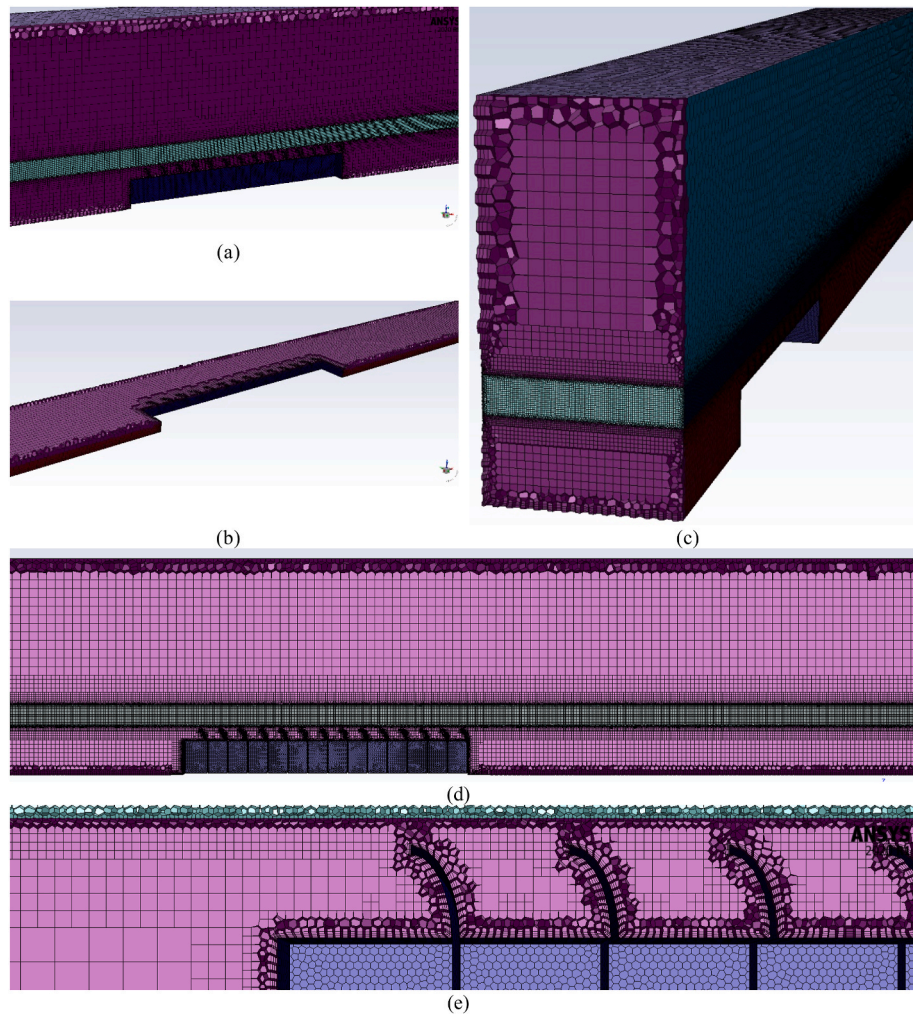


Fig. 23. Screenshots of the mesh configuration of the symmetric 3D CNWT model.

3.2. Wave-structure interaction tests

Wave-structure interaction is a complex hydrodynamic process in which non-linear dissipative phenomena occur. The impinging wave interacts with a complex structure composed by a rectangular parallelepiped with sharp edges covered by an ensemble of fourteen exterior stay vanes with smooth curves. The experimental tests reported in Ref. [25] show that the resulting wave state is irregular (e.g., Fig. 13 (b)) and of random nature. Considering that no information about the exact time period after the activation of the wavemaker that corresponds the upstream (Fig. 13a) and downstream (Fig. 13b) measured time series as

provided by Lopes de Almeida and Martinho [25], a comparison based on superimposition of the results was not possible. Therefore, an alternative criterion was used, based on the evaluation of the zero order moments of the resulting wave spectra, which are proportional to the wave state energy density. According to this criterion, if a good numerical model of the wave-structure interaction is achieved, then the numerical and experimental zero order moments of the resulting wave state should match. From the experimental database analysis, five incident wave heights from approximately 0.02 m–0.06 m, with a period of $T = 0.86$ s, propagating at a water depth of $d = 0.275$ m, were established for the present study. The corresponding wave-structure

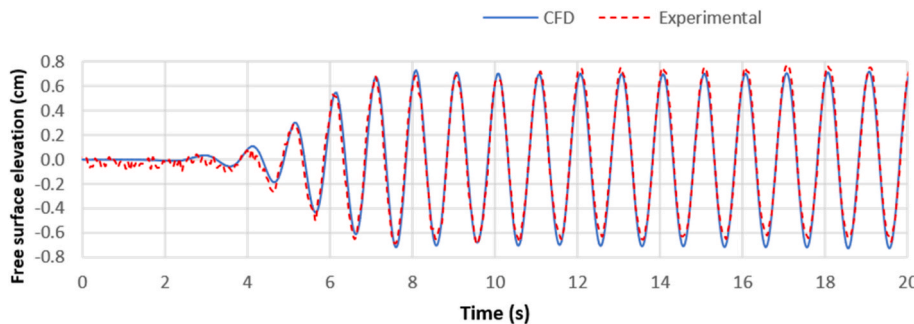


Fig. 24. Comparison of numerical (blue line) and experimental (dashed red line) free surface elevation time series at wave probe WR1 (see Fig. 4) for $T = 0.860$ s, $H = 0.014$ m and $d = 0.275$ m (wave-only test case 1).

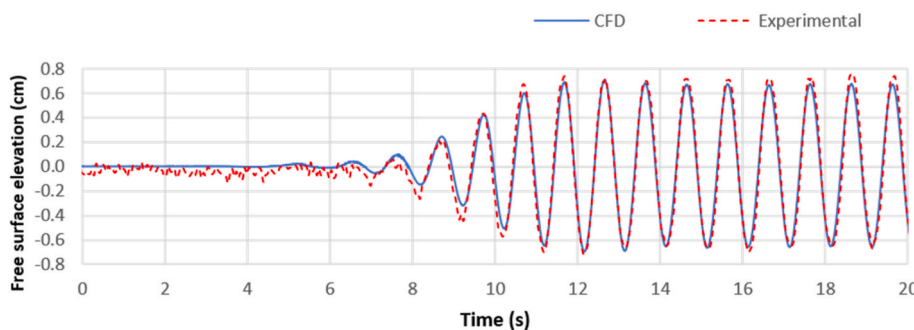


Fig. 25. Comparison of numerical (blue line) and experimental (dashed red line) free surface elevation time series at wave probe WR2 (see Fig. 4) for $T = 0.860$ s, $H = 0.014$ m and $d = 0.275$ m (wave-only test case 1).

interaction was then computed using the 3D CNWT model. The REEFS WEC was modelled without the turbine module and with the inner flow blocked to replicate the non-operating conditions established in the experimental study in which the passive coastal protection potential of the device was investigated. The numerical wave gauges (WP'1 and WP'2) were implemented at the same positions of the corresponding experimental wave gauges (i.e., P1 and P2&3 in Fig. 11). At each wave gauge the variation of the free surface elevation was numerically measured by monitoring the variation of the z-position of the water volume fraction $\alpha_{VF} = 0.5$ iso-surface. All numerical models were run for a total simulation time of $t_s = 30$ s, ensuring flow stabilisation for reliable data acquisition. A preliminary analysis demonstrated that a time step of $T/200$ was not enough to capture the complex phenomena involved in the wave-structure interaction. Thus, a smaller time step of $T/400$ was implemented. The numerical free surface elevation time series from wave gauges WP'1 and WP'2 (e.g., Fig. 27) were processed using the spectral analysis methodology mentioned in Section 2.1.4.

Fig. 28 presents a comparison between the experimental and numerical zero order spectral moments, m_0 . The upstream experimental

(P1 - Exp) and numerical (WP'1 - CFD) values are considerably higher than the corresponding downstream experimental (P2&P3 - Exp) and numerical (WP'2 - CFD) values, as should be expected given the approximated wave energy dissipation originated by the submerged breakwater effect of the REEFS model. A small fraction of dissipated energy should be attributed to reflected waves; however, a detailed assessment of the shore protection capabilities of the REEFS is not an objective of the present study. The theoretical curve of m_0 ($m_0 = \frac{1}{8}H^2$) is very well aligned with the incident wave zero order spectral moments (P1 - Exp) and (WP'1 - CFD), showing that the incident experimental and numerical regular waves were indeed following linear behaviour, with the second order term of Stokes 2nd order waves being nearly negligible. The downstream experimental (P2&P3 - Exp) and numerical (WP'2 - CFD) zero order moments are well aligned, showing that the energy density of the wave state resulting from wave-structure interaction was well modelled by the CNWT model. Although this was not the purpose of the present study, an average variation of the wave energy density of 67%, between upstream and downstream relative positions, was calculated, this being in accordance with the 68% determined experimentally

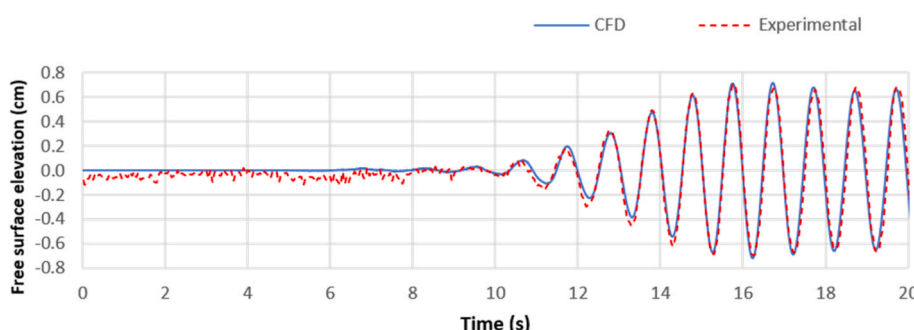


Fig. 26. Comparison of numerical (blue line) and experimental (dashed red line) free surface elevation time series at wave probe WR3 (see Fig. 4) for $T = 0.860$ s, $H = 0.014$ m and $d = 0.275$ m (wave-only test case 1).

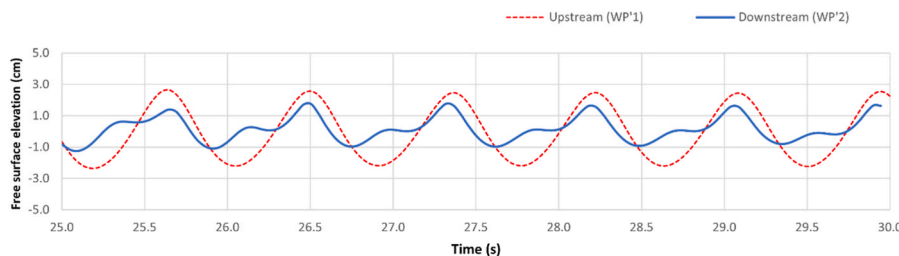


Fig. 27. Numerical results from the 3D CNWT model with a mesh of approximately 4.2 million cells and a time step of T/400. (a) Upstream (WP'1) regular wave profile and (b) downstream (WP'2) irregular wave profile from last 5 s of simulation time, for an incident wave with $T = 0.86$ s, height, $H = 0.05$ m, and depth, $d = 0.275$ m.

by Lopes de Almeida and Martinho [25].

In the approach of the incoming waves to the REEFS, part of the energy was locally dissipated and reflected, while the remaining energy was transmitted through the submerged breakwater. Similar to Lopes de Almeida and Martinho [25], the REEFS impact on wave transformation was characterized by classical parameters: reflection (K_r), dissipation (K_d) and transmission (K_t) coefficients.

The reflection coefficient can be defined as the ratio of the reflected wave height, H_r , to the incident wave height, H_i ,

$$K_r = \frac{H_r}{H_i} \quad (12)$$

The numerical incident and reflected waves were estimated using the well-known Goda's method (Goda and Suzuki [45]), through the analysis of the free surface elevation time series at two fixed upstream water level wave gauges. In agreement with laboratory set-up and considering the limitations of Goda's method for the relative gauge spacing, the same P0 and P1 positions (Figs. 11 and 12) were adopted to collect the required numerical data. The Discrete Fourier Transform (DFT) technique was implemented to compute A_1 , B_1 , A_2 and B_2 amplitudes of the Goda's method, obtaining incident and reflected wave amplitudes.

The numerical reflection coefficients, for the same five numerical simulated incident waves from Fig. 28, are presented in Fig. 29.

From the results presented in Fig. 29, it is verified that wave reflection increased with wave height, what was expected considering

that the relative submergence decreases, i.e. the REEFS obstruction to incoming waves is higher.

Based on the estimation of the transmitted wave height, H_t (Peña et al. [46]), the transmission coefficient can be calculated by the following equation,

$$K_t = \frac{H_t}{H_i} \quad (13)$$

As verified in Fig. 27, irregular waves were originated in the lee of the REEFS, what makes it difficult to identify the transmitted wave height. Liang et al. [47] proposed to calculate the transmission coefficient based on the wave energy spectrum of the incident and transmitted waves,

$$K_t = \frac{\sqrt{m_{0,t}}}{\sqrt{m_{0,i}}} \quad (14)$$

where $m_{0,t}$ and $m_{0,i}$ are the 1st order moments of the transmitted and incident wave energy spectrum, respectively. The calculated 1st order moments collected at WP'1 (incident wave) and WP'2 (transmitted wave), shown in Fig. 28, were used to compute the corresponding transmission coefficient values, see Fig. 30.

While wave reflection increased with wave height, the transmitted wave coefficient decreased with wave height (Fig. 30).

Based on the energy conservation law, the following equation can be derived (Seeling and Ahrens [48] and Liang et al. [47]),

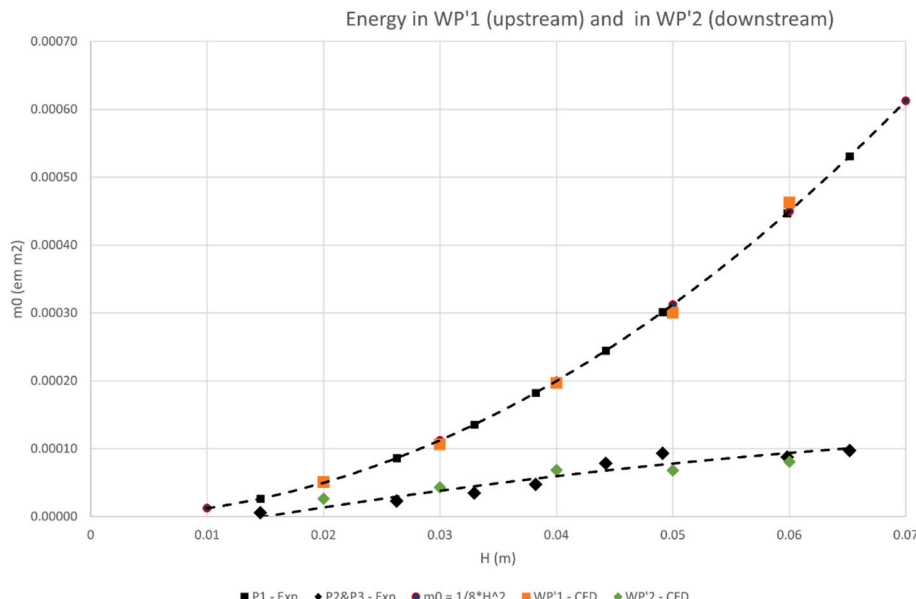


Fig. 28. Experimental and CFD comparison of average wave energy density for $T = 0.86$ s, at upstream (P1 – WP'1) and downstream (P2&P3 – WP'2) relative positions of the REEFS WEC model.

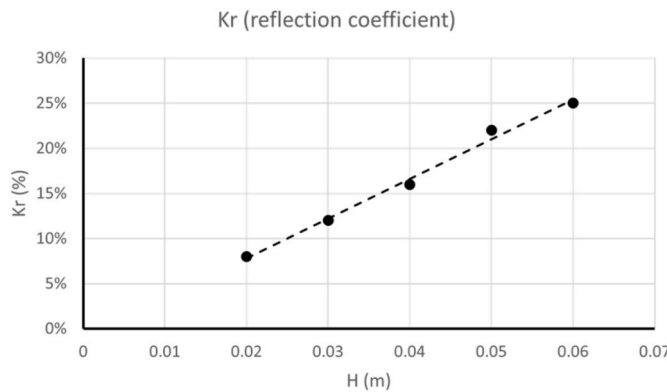


Fig. 29. Reflection coefficient, K_r , variation with wave height, for a period of $T = 0.86$ s, with a constant submergence of $S = 0.125$ m.

$$K_r^2 + K_t^2 + K_d^2 = 1 \quad (15)$$

Therefore, the dissipation coefficient was calculated, and the results are presented in Fig. 31.

Comparing the average coefficient values calculated numerically (from Figs. 29–31), where $K_r = 17\%$, $K_t = 57\%$ and $K_d = 79\%$, with the laboratory ones, for the same wave period of $T = 0.86$ s, from Lopes de Almeida and Martinho [25], $K_r = 14\%$, $K_t = 46\%$ and $K_d = 88\%$, a root mean square of 19% for the global relative difference between CFD and laboratorial results can be computed. This can be considered an acceptable agreement given the inherent different nature of the two studies, the unmatchable monitoring time instants and the different duration of the wave experiments which was much shorter in the CFD due to the high computational costs.

The reliability of the numerical model was also assessed using a comparison analysis of the numerical and experimental wave surface transformation in the REEFS zone. This approach is also of upmost importance to globally check the stability and correctness of the hydrodynamic behaviour of the CFD model. Fig. 32 presents an example with numerical (left side) and experimental (right side) global water surface above the REEFS device, for an incident wave with $T = 0.860$ s, $H = 0.050$ m and $d = 0.275$ m propagating from left to the right. In Fig. 32 (a), it is possible to see that the combined effect of shoaling and high drag leads to the formation of partial wave breaking, visible as a small protuberance at the centre of both images. In Fig. 32 (b), two crests can be observed. The downstream crest of Fig. 32 (b) presents a horse-shoe shape, resulting from the spreading of the wave breaking identified in Fig. 32 (a). The upstream crest of Fig. 32 (b) presents an embryonic central protuberance that will evolve to the protuberance previously identified in Fig. 32 (a). Between these two crests there is a depression

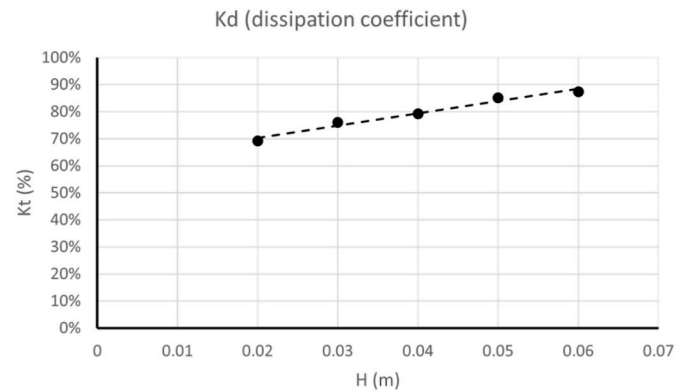


Fig. 31. Dissipation coefficient, K_d , variation with wave height for a period of $T = 0.86$ s, with a constant submergence of $S = 0.125$ m.

that occupies most of the surface above the REEFS device. To some extent, all the described features are simultaneously identifiable in both the numerical (left side) and experimental (right side) images.

A complementary snapshot comparison using side views was also accomplished. In Fig. 33 (a) and (b), examples of the same incident wave seen in Fig. 32 are presented. In all the images in Fig. 33 a protuberance caused by wave breaking located above the downstream part of the device is clearly identifiable, preceded by a long trough with a tail depression located above the initial upstream part of the device. The positioning and magnitude of the protuberance, as well as the positioning and magnitude of the trough, in the numerical simulations (upper images), match quite well with the experimental tests (lower images). A quantitative analysis of the experimental envelope of the free surface elevation is also possible, using the well-known REEFS height as reference. At the trough, the numerical depth of the protuberance shows a deviation from experimental of approximately 4%, while a maximum deviation of 3% was found for height at the top of the crest.

Due to the curved shape of the stay vanes, horizontal backwards water flow was concentrated in the trough zone, causing a localised velocity increase. Energy conservation requires that this localised kinetic energy increase must be compensated by a localised pressure drop; this is commonly known as the Venturi effect. A close look at the experimental tests (Fig. 33) demonstrates the presence of this effect, easily identifiable as the depression zone at the tail of the trough. This phenomenon is clearly captured by CFD (Fig. 34). The velocity vectors show a strong magnitude in a backward direction under the trough (Fig. 34a), while an opposite direction is identified under the crest (Fig. 34b). The basic working principles of the REEFS, i.e., the capturing the spatial differentials of kinetic and pressure energy in the water mass by the natural opening and closing of the valves, can also be identified in the snapshots in Fig. 34. Under the crest, the velocity vectors point inward of the REEFS, forcing the opening of the valves, while under the trough an outward movement is observed, closing the valves.

The contour plots of the velocity field around the REEFS (Fig. 35), at different planes, enable a better assessment of the wave-structure interaction phenomena. For example, local recirculation zones can be observed next to the edges of the exterior stay vanes, generating vorticity phenomena. This type of analysis can be helpful for the optimisation process, for example in the improvement of the REEFS shore protection performance based on the design of the exterior stay vanes.

The potential of the CFD approach for wave-structure problems is well expressed by the analysis presented here. The capacity to solve complex 3D fluid flows around structures, with detailed information about fluid properties such as velocity and pressure, as functions of space and time, offers huge advantages for the future functioning (wave power and shore protection) and structural optimisation of the REEFS wave energy converter, as a precursor to the jump to physical large-scale tests. However, it is important to mention that model verification and

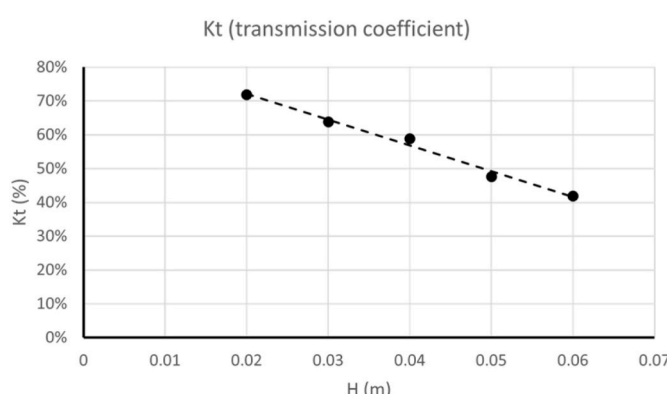


Fig. 30. Transmission coefficient, K_t , variation with wave height for a period of $T = 0.86$ s, with a constant submergence of $S = 0.125$ m.

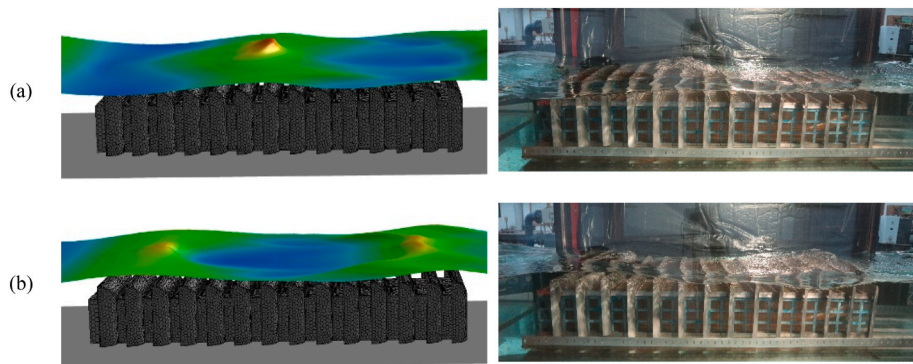


Fig. 32. Snapshot comparison between CFD (left side) and experimental (right side) free surface above REEFS device for an incident wave with $T = 0.860$ s, $H = 0.050$ m at $d = 0.275$ m.

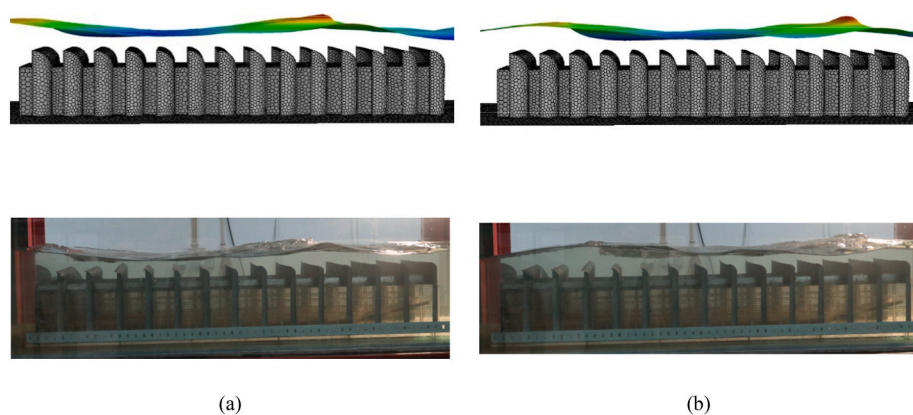


Fig. 33. Snapshot comparison between CFD (upper images) and experimental (lower images) lateral views of the free surface above REEFS device for an incident wave with $T = 0.860$ s, $H = 0.050$ m at $d = 0.275$ m.

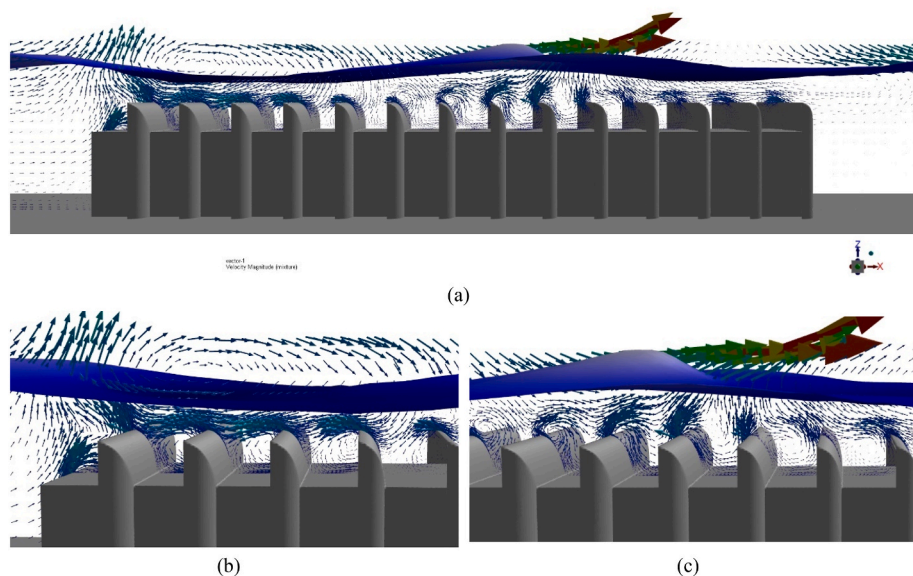


Fig. 34. CFD snapshots of the $\alpha_{VF} = 0.5$ iso-surface (free surface) and the vector representation of the velocity, at the plane $y = 0$, above REEFS device for an incident wave with $T = 0.860$ s, $H = 0.050$ m at $d = 0.275$ m.

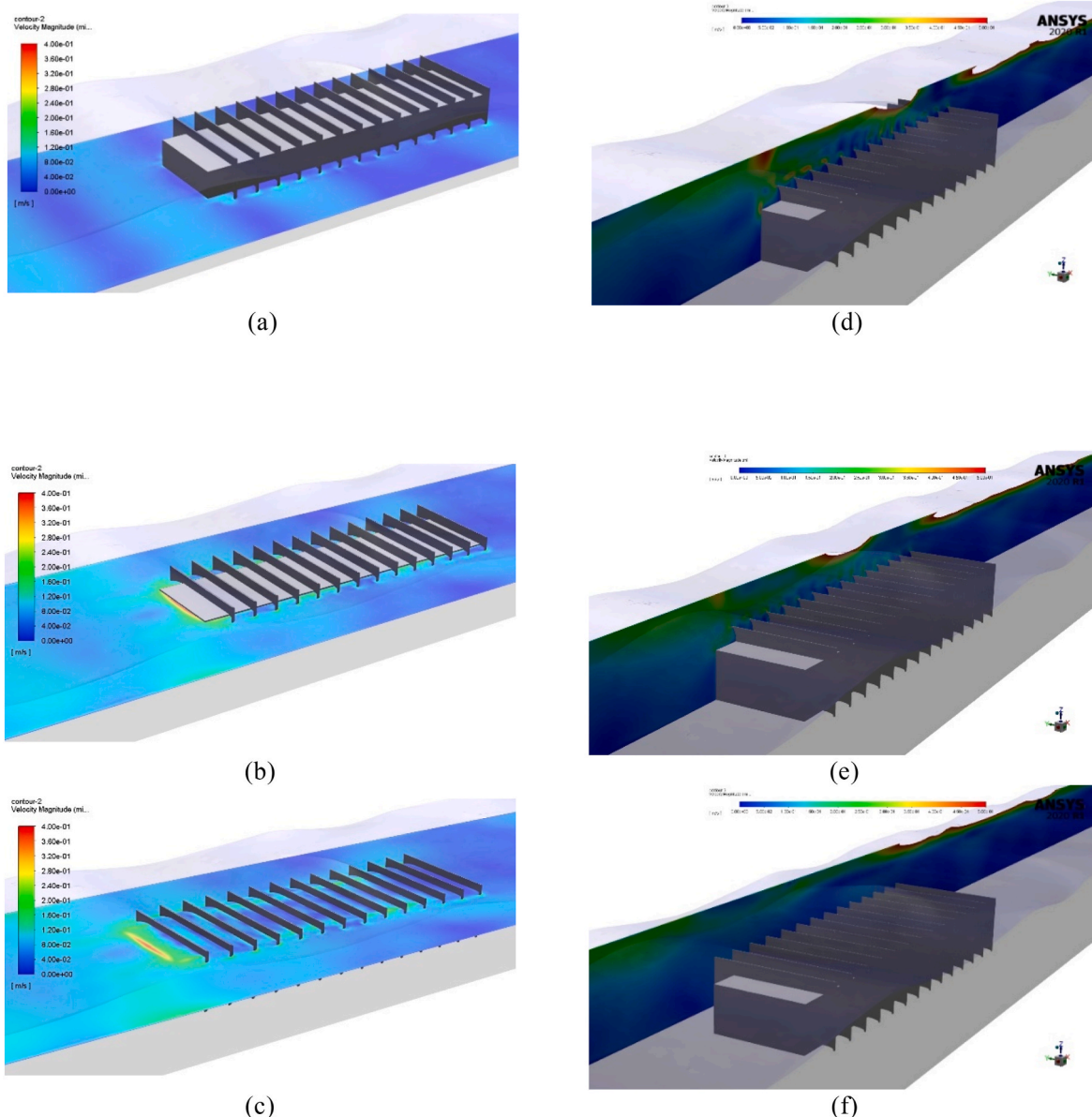


Fig. 35. Snapshots of velocity contour plots at different planes: (a) $z = 0.05$ m (b) $z = 0.15$ m (c) $z = 0.17$ m (d) $y = 0.00$ m (e) $y = 0.15$ m (f) $y = 0.30$ m, above REEFS device for an incident wave with $T = 0.860$ s, $H = 0.050$ m at $d = 0.275$ m.

validation based on experimental data, using small scale models, must be always performed.

4. Conclusions

This article documents the development and exploration of the capabilities of a 3D CNWT model of a novel multipurpose wave energy converter, REEFS, using experimental data for comparison. The following conclusions can be drawn from the results:

- The complexity of REEFS geometry requires a step-by-step approach where an initial numerical calibration based on wave-only test cases is suggested.
- Spatial and temporal discretisation are case dependent and should be assessed by convergence studies.
- The numerical free surface elevations and wave energy densities showed acceptable agreements with laboratory measured data, as well as reflection, transmission, and dissipation coefficients.

- The implemented CNWT model, based on RANS-VOF approach, showed to be computationally feasible and with acceptable accuracy, making it a possible alternative computational tool to support future studies of the novel multipurpose REEFS wave energy converter.

CRediT authorship contribution statement

D. Oliveira: Conceptualization, Investigation, Formal analysis, Writing – original draft. **J.P.P.G. Lopes de Almeida:** Conceptualization, Supervision, Writing – review & editing. **A. Santiago:** Conceptualization, Supervision, Writing – review & editing. **C. Rigueiro:** Conceptualization, Supervision, Writing – review & editing.

Declaration of competing interest

The authors declare that they have no known competing financial interests or personal relationships that could have appeared to influence the work reported in this paper.

Acknowledgements

This work was supported by the Foundation for Science and Technology (FCT) through the individual research grant [SFRH/BD/118715/2016]; by FCT/MCTES through national funds (PIDDAC) under the R&D Unit Institute for Sustainability and Innovation in Structural Engineering (ISISE), under reference [UIDB/04029/2020], and under the R&D Unit MARE – Marine and Environmental Sciences Centre.

References

- [1] K. Gunn, C. Stock-Williams, Quantifying the global wave power resource, *Renew. Energy* 44 (2012) 296–304, <https://doi.org/10.1016/j.renene.2012.01.101>.
- [2] World Energy Council, World energy Resources: marine energy, Available on line at, <https://www.worldenergy.org/>, 2016. (Accessed 16 September 2019).
- [3] EU-FP7 MaRINET Project, Deliverable D2.23: Review of Tow Tank Limitations, 2014.
- [4] C. Windt, J. Davidson, J. Ringwood, High-fidelity numerical modelling of ocean wave energy systems: a review of computational fluid dynamics-based numerical wave tanks, *Renew. Sustain. Energy Rev.* 93 (2018) 610–630, <https://doi.org/10.1016/j.rser.2018.05.020>.
- [5] C. Eskilsson, J. Palm, L. Bergdahl, On numerical uncertainty of VOF-RANS simulations of wave energy converters through V&V techniques, in: 12th EWTEC - Proceedings of the 12th European Wave and Tidal Energy Conference: 27th Aug -1st Sept 2017, Cork, Ireland [1021] Technical Committee of the European Wave and Tidal Energy Conference. European Wave and Tidal Energy Conference Series Vol. 12, 2017.
- [6] W. Wang, M. Wu, J. Palm, C. Eskilsson, Estimation of numerical uncertainty in computational fluid dynamics simulations of a passively controlled wave energy converter, *Proc. Inst. Mech. Eng. Part M J. Eng. Marit. Environ.* 232 (2018) 71–84, <https://doi.org/10.1177/1475090217726884>.
- [7] L. Eça, G. Vaz, M. Hoekstra, A verification and validation exercise for the flow over a backward facing step, in: *Proceedings of the V European Conference on Computational Fluid Dynamics*, 2010.
- [8] M.N. Gomes, L.A. Isoldi, C.R. Olinto, L.A.O. Rocha, J.A. Souza, Computational modeling of a regular wave tank, in: *Proceedings of the Third Southern Conference on Computational Modelling*, 2009, pp. 60–65, <https://doi.org/10.1109/MCSUL.2009.27>.
- [9] M.C. Silva, M. de A. Vitola, W.T.P. Pinto, C.A. Levi, Numerical Simulation of monochromatic wave generated in laboratory: validation of a CFD code, in: 23th Congresso Nacional de Transporte Aquaviário, Construção Naval e Offshore, Rio de Janeiro, Brazil, 2010, pp. 25–29, <https://doi.org/10.1111/j.1748-720X.2012.00715.x>.
- [10] F.M. Marques Machado, A.M. Gameiro Lopes, A.D. Ferreira, Numerical simulation of regular waves: optimization of a numerical wave tank, *Ocean Eng.* 170 (2018) 89–99, <https://doi.org/10.1016/j.oceaneng.2018.10.002>.
- [11] A. Miquel, A. Kamath, M. Alagan Chella, R. Archetti, H. Bihs, Analysis of different methods for wave generation and absorption in a CFD-based numerical wave tank, *J. Mar. Sci. Eng.* 6 (2018) 73, <https://doi.org/10.3390/jmse6020073>.
- [12] H. Bihs, A. Kamath, M. Alagan Chella, A. Aggarwal, Ø.A. Arntsen, A new level set numerical wave tank with improved density interpolation for complex wave hydrodynamics, *Comput. Fluids* 140 (2016) 191–208, <https://doi.org/10.1016/j.compfluid.2016.09.012>.
- [13] C. Windt, J. Davidson, P. Schmitt, J. Ringwood, On the assessment of numerical wave makers in CFD simulations, *J. Mar. Sci. Eng.* 7 (2019) 47, <https://doi.org/10.3390/jmse7020047>.
- [14] W. Finnegan, J. Goggins, Numerical simulation of linear water waves and wavestructure interaction, *Ocean Eng.* 43 (2012) 23–31, <https://doi.org/10.1016/j.oceaneng.2012.01.002>.
- [15] S.Y. Kim, K.M. Kim, J.C. Park, G.M. Jeon, H.H. Chun, Numerical simulation of wave and current interaction with a fixed offshore substructure, *Int. J. Nav. Archit. Ocean Eng.* 8 (2016) 188–197, <https://doi.org/10.1016/j.ijnaoe.2016.02.002>.
- [16] S.K. Chakrabarti, W.A. Tam, Interaction of waves with large vertical cylinder, *J. Ship Res.* 19 (1975) 23–33.
- [17] J.R. Morison, J.W. Johnson, S.A. Schaaf, The force exerted by surface waves on piles, *J. Petrol. Technol.* 2 (1950) 149–154, <https://doi.org/10.2118/950149-G>.
- [18] D.D. Prasad, M.R. Ahmed, Y.H. Lee, R.N. Sharma, Validation of a piston type wavemaker using Numerical Wave Tank, *Ocean Eng.* 131 (2017) 57–67, <https://doi.org/10.1016/j.oceaneng.2016.12.031>.
- [19] C. Windt, J. Davidson, E.J. Ransley, D. Greaves, M. Jakobsen, M. Kramer, J. V. Ringwood, Validation of a CFD-based numerical wave tank model for the power production assessment of the wavestar ocean wave energy converter, *Renew. Energy* 146 (2020) 2499–2516, <https://doi.org/10.1016/j.renene.2019.08.059>.
- [20] C. Windt, N. Faedo, D. García-Violini, Y. Peña-Sánchez, J. Davidson, F. Ferri, J. V. Ringwood, Validation of a CFD-Based numerical wave tank model of the 1/20th scale wavestar wave energy converter, *Fluids* 5 (3) (2020), 112, <https://doi.org/10.3390/fluids5030112>.
- [21] B. Di Paolo, J.L. Lara, G. Barajas, I.J. Losada, Waves and structure interaction using multi-domain couplings for Navier-Stokes solvers in OpenFOAM®. Part II: validation and application to complex cases, *Coast. Eng.* 165 (2021), 103818, <https://doi.org/10.1016/j.coastaleng.2020.103818>.
- [22] J.L. Lara, G. Barajas, I.J. Losada, Wave and structure interaction using multi-domain couplings for Navier-Stokes solvers in OpenFOAM®. Part I: implementation and validation, *Coast. Eng.* 164 (2021), 103799, <https://doi.org/10.1016/j.coastaleng.2020.103799>.
- [23] J.P.G. Lopes de Almeida, REEFS: an artificial reef for wave energy harnessing and shore protection – a new concept towards multipurpose sustainable solutions, *Renew. Energy* 114 (2017) 817–829, <https://doi.org/10.1016/j.renene.2017.07.076>.
- [24] J.P.G. Lopes de Almeida, B. Mujtaba, A.M. Oliveira Fernandes, Preliminary laboratorial determination of the REEFS novel wave energy converter power output, *Renew. Energy* 122 (2018) 654–664, <https://doi.org/10.1016/j.renene.2018.01.030>.
- [25] J.P.G. Lopes de Almeida, M.F.E. Santos Martinho, Experimental evaluation of the shore protection potential of the novel REEFS wave energy converter, *Ocean Eng.* 217 (2020), 107918, <https://doi.org/10.1016/j.oceaneng.2020.107918>.
- [26] J.P.G. Lopes de Almeida, J.R.C.B. Abrantes, J.G.S.E. Bento, A simplified model for expedited computational assessment of the novel REEFS wave energy converter power output, *Renew. Energy* 157 (2020) 43–54, <https://doi.org/10.1016/j.renene.2020.04.128>.
- [27] J. Havn, *Wave Loads on Underwater Protection Covers*, MSc Thesis, 2011.
- [28] F.M. Seibt, E.C. Couto, E.D. dos Santos, L.A. Isoldi, L.A.O. Rocha, P.R. de F. Teixeira, Numerical study on the effect of submerged depth on the horizontal plate wave energy converter, *China Ocean Eng.* (2014), <https://doi.org/10.1007/s13344-014-0056-x>.
- [29] E.J. Ransley, D. Greaves, A. Raby, D. Simmonds, M. Hann, Survivability of wave energy converters using CFD, *Renew. Energy* 109 (2017) 235–247, <https://doi.org/10.1016/j.renene.2017.03.003>.
- [30] C. Windt, J. Davidson, B. Akram, J.V. Ringwood, Performance assessment of the overset grid method for numerical wave tank experiments in the openfoam environment, in: *Proceedings of the ASME 2018 37th International Conference on Ocean, Offshore and Arctic Engineering*, 10, 2018, OMAE2018-77564, <https://doi.org/10.1115/OMAE2018-77564>.
- [31] DHI Water & Environment, DHI Wave Synthesizer User Guide, 2007. Denmark, www.dhi.dk.
- [32] H.R. Wallingford, Wave Gauge Monitor System and Wave Probe Description, 2020 (accessed March 10, 2020), <http://equipit.hrwallingford.com/products/wave-gauges/twin-wire-wave-probe-300mm>.
- [33] H.R. Wallingford, Wave Data Acquisition and Analysis Software Description, 2020 (accessed March 10, 2020), <http://equipit.hrwallingford.com/products/software/hr-daq-software>.
- [34] R.G. Dean, R.A. Dalrymple, *Water Wave Mechanics for Engineers and Scientists*, WORLD SCIENTIFIC, 1991, <https://doi.org/10.1142/1232>.
- [35] M. Rahman, *Fundamentals Concerning Stokes Waves*, 1996.
- [36] Microsoft, Excel User Guide Support. <https://support.office.com/>, 2019.
- [37] J.H. Ferziger, M. Perić, *Computational Methods for Fluid Dynamics*, 1996, <https://doi.org/10.1007/978-3-642-97651-3>.
- [38] ANSYS, *ANSYS Fluent User's Guide*, 2020.
- [39] C.W. Hirt, B.D. Nichols, Volume of fluid (VOF) method for the dynamics of free boundaries, *J. Comput. Phys.* 39 (1) (1981) 201–225, [https://doi.org/10.1016/0021-9991\(81\)90145-5](https://doi.org/10.1016/0021-9991(81)90145-5).
- [40] I.R. Park, K.S. Kim, J. Kim, S.H. Van, A volume-of-fluid method for incompressible free surface flows, *Int. J. Numer. Methods Fluid.* 61 (12) (2009) 1331–1362, <https://doi.org/10.1002/fld.2000>.
- [41] A. Elhanafi, A. Fleming, G. Macfarlane, Z. Leong, Numerical energy balance analysis for an onshore oscillating water column–wave energy converter, *Energy* 116 (2016) 539–557, <https://doi.org/10.1016/j.energy.2016.09.118>.
- [42] ANSYS Academic Research, *ANSYS Fluent Theory Guide, ANSYS Help Syst.*, 2020.
- [43] R. Perić, M. Abdel-Maksoud, Reliable damping of free-surface waves in numerical simulations, *Ship Technol. Res.* 63 (1) (2016) 1–13, <https://doi.org/10.1080/09377255.2015.1119921>.
- [44] E.P.D. Mansard, The measurement of incident and reflected spectra using a least squares method, *Sydney, Aust. Mar. 23-28, 1980*. 1, New York, U.S.A., Am. Soc. Civ. Engrs., in: *Proc. Seventeenth Coast. Engng. Conf. Part 1*, 1981 <https://doi.org/10.1061/9780872622647.008> (Chapter 8) (1981) 154–172.
- [45] Y. Goda, T. Suzuki, Estimation of incident and reflected waves in random wave experiments, *Coast. Eng. Proc.* 1 (1976) 47, <https://doi.org/10.9753/icce.v15.47>.
- [46] E. Peña, J. Ferreras, F. Sanchez-Tembleque, Experimental study on wave transmission coefficient, mooring lines and module connector forces with different designs of floating breakwaters, *Ocean Eng.* 38 (10) (2011) 1150–1160, <https://doi.org/10.1016/j.oceaneng.2011.05.005>.
- [47] C. Liang, Q. Gu, G. Huang, N. Zhang, Effect of RN number on the dissipation performance of twin-plate breakwater, *Ocean Eng.* 195 (2020), 106672, <https://doi.org/10.1016/j.oceaneng.2019.106672>.
- [48] W.N. Seelig, J.P. Ahrens, *Estimation of Wave Reflection and Energy Dissipation Coefficients for Beaches, Revetments, and Breakwaters*, U.S. Army Coast. Eng. Res. Center, 1981. Tech. Pap.